



HAL
open science

Sea surface temperature impact on diurnal cycle and seasonal evolution of the Guinea Coast Rainfall in boreal spring and summer

Manuel Tanguy, Gaëlle de Coëtlogon, Laurence Eymard

► To cite this version:

Manuel Tanguy, Gaëlle de Coëtlogon, Laurence Eymard. Sea surface temperature impact on diurnal cycle and seasonal evolution of the Guinea Coast Rainfall in boreal spring and summer. *Monthly Weather Review*, 2022, (in press). 10.1175/MWR-D-21-0155.1 . insu-03542344v1

HAL Id: insu-03542344

<https://insu.hal.science/insu-03542344v1>

Submitted on 27 Jan 2022 (v1), last revised 21 Dec 2022 (v2)

HAL is a multi-disciplinary open access archive for the deposit and dissemination of scientific research documents, whether they are published or not. The documents may come from teaching and research institutions in France or abroad, or from public or private research centers.

L'archive ouverte pluridisciplinaire **HAL**, est destinée au dépôt et à la diffusion de documents scientifiques de niveau recherche, publiés ou non, émanant des établissements d'enseignement et de recherche français ou étrangers, des laboratoires publics ou privés.

1 **Sea surface temperature impact on diurnal cycle and seasonal evolution of**
2 **the Guinea Coast Rainfall in boreal spring and summer**

3 Manuel Tanguy ^a, Gaëlle de Coëtlogon^a and Laurence Eymard ^a

4 ^a *LATMOS-IPSL, Sorbonne Université*

5 *Corresponding author:* Manuel Tanguy, manuel.tanguy@latmos.ipsl.fr – Université Paris Saclay,
6 4 place Jussieu, 75252 Paris cedex 05, France

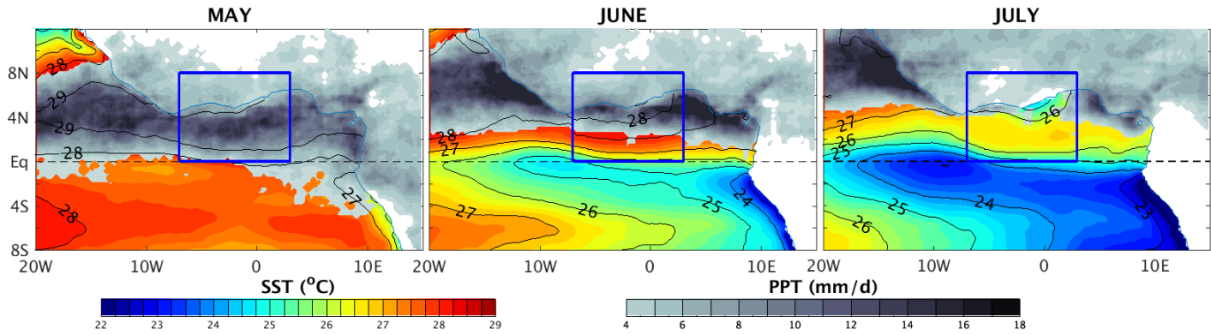
7 ABSTRACT: ERA5 reanalyses and observations of convective clouds and precipitation are used
8 over the northern Gulf of Guinea between 7W and 3E to study the influence of ocean surface
9 temperature and land-sea temperature gradient on Guinea Coast Rainfall (GCR) in boreal spring
10 and summer. Seasonal composites are calculated around two dates indexing the onset (T_{ref})
11 and demise (T_{end}) of the GCR: T_{ref} corresponds to the emergence of the equatorial upwelling
12 in boreal spring, which "pushes" the zonal precipitation belt northward against the Guinea coast.
13 T_{end} characterizes the emergence of the coastal upwelling in July, which is known to coincide
14 with the beginning of the "little dry season" that lasts until September. Along the Guinea Coast,
15 the diurnal cycle of the air-sea temperature gradient controls precipitation through the land-sea
16 breeze, which explains why precipitation reaches its maximum around noon over the ocean, and
17 in the late afternoon over the continent. The emergence of the Guinea Coast upwelling in July
18 induces a weakening of southerlies on a seasonal scale, and a weaker land breeze on a diurnal
19 scale: it induces a decrease in the convergence of humidity transport across the coast and in coastal
20 oceanic precipitation. Therefore, the GCR is seasonally controlled by the latitude of the maximum
21 tropospheric water vapor content and the annual cycle of the West African Monsoon, but the ocean
22 surface temperature is responsible for the abruptness of its onset via the intensification of the
23 equatorial upwelling around the end of May, and possibly of its demise as well via the emergence
24 of the coastal upwelling by early July.

25 **1. Introduction**

26 The correct representation of precipitation in numerical atmospheric models remains one of the
27 most important challenges in climate physics (IPCC 2007, Bony et al. (2015)), particularly in West
28 Africa, where precipitation is poorly represented in models (Sylla et al. 2013; Roehrig et al. 2013;
29 Harlaß et al. 2015; Steinig et al. 2018; Kniffka et al. 2020; Sow et al. 2020; Kouadio et al. 2018). A
30 better understanding of processes controlling precipitation is therefore needed in order to improve
31 its representation.

39 Precipitation in West Africa is primarily controlled by the monsoon, driven by a huge meridional
40 contrast in temperature and humidity between eastern Tropical Atlantic and the dry continent
41 further north (Parker et al. 2017). In response to the annual solar cycle, precipitation latitude
42 exhibits a strong seasonal cycle (Peyrillé et al. 2007; Hagos and Cook 2007; Thorncroft et al.
43 2011; Maranan et al. 2018). The zonal band of precipitation is centred on the northern Gulf of
44 Guinea and Guinea Coast (around 5N) between late April and early July (see Figure 1 for May and
45 June precipitation). This near-coastal oceanic precipitation, named the "Guinea Coast Rainfall" (or
46 GCR, Nguyen et al. (2011a)), shifts northward in late June / early July and brings precipitation over
47 the Sahel (see Figure 1 for July precipitation) until September, during the monsoon demise, when
48 the Guinea Coast countries experience a second rainfall peaking in October-November (Sultan and
49 Janicot 2003; Zhang and Cook 2014). Between July and September, precipitation over the coastal
50 region is scarce between 12W and 7E and is referred to as the "Little Dry Season" (Adejuwon and
51 Odekunle 2006; Fink et al. 2017; Wainwright et al. 2019). Precipitation is mainly localized over
52 the ocean during the rest of the year. The countries along the northern coast of the Gulf of Guinea
53 therefore experience two rainy seasons and two dry seasons per year; the near-coastal precipitation
54 in June / early July is of particular interest, because it may condition the onset of summer monsoon
55 in the Sahel through the control of the meridional gradient of soil moisture (Zheng et al. 1999).
56 Furthermore, its interannual variability has been shown to be largely controlled by sea surface
57 temperature (SST) in the eastern Tropical Atlantic (Giannini et al. 2003; Polo et al. 2008; Losada
58 et al. 2010; Suárez-Moreno et al. 2018). However, few previous studies have conducted a thorough
59 investigation of the mechanisms linking SST and the onset or demise of GCR on intraseasonal
60 timescales.

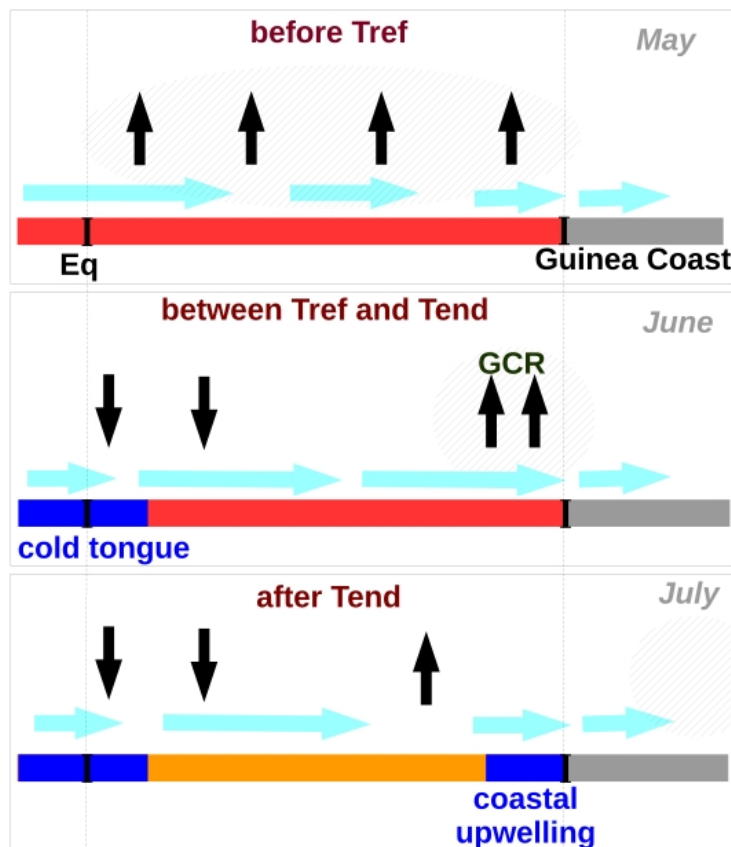
61



32 FIG. 1. 2008-2015 SST (Reynolds product, color shading and black contours from 24°C to 27°C, intervals of
 33 1°C) and precipitation larger than 4 mm/d (TRMM, gray shading) in May (left), June (middle) and July (right).
 34 Blue frame delimits the region of scrutiny, black dashed line indicates the equator.

62 The northward migration of the zonal band of precipitation, also known as the “monsoon jump”
 63 around 24 June (Sultan and Janicot 2003), and the variability of precipitation in boreal summer,
 64 have been extensively studied in the international African Monsoon Multidisciplinary Analysis
 65 (AMMA) project (Redelsperger et al. 2006) and shown to be primarily controlled by the continental
 66 surface (Wang and Eltahir 2000; Thorncroft et al. 2011). However, precipitation is also controlled
 67 by SST in the Gulf of Guinea, where a strong equatorial upwelling emerges in boreal spring and
 68 summer (see blue bands in June and July, in figure 2), increasing meridional thermal gradients at the
 69 surface (Okumura and Xie 2004; Caniaux et al. 2011; Nguyen et al. 2011a; Nnamchi and Li 2011;
 70 Leduc-Leballeur et al. 2013; Crespo et al. 2019; Worou et al. 2020). Using numerical simulations,
 71 Meynadier et al. (2015) showed that the emergence of equatorial upwelling controls the GCR
 72 onset in late May, through an increase in surface winds north of the equator and a convergence of
 73 humidity near the Guinea Coast, represented by monsoon flow and coastal convergence increases
 74 in figure 2. In addition, a strong coastal upwelling appears along the Guinea Coast in boreal
 75 summer (July to September), where the SST decreases from about 30°C in May to 24-25°C in
 76 August (Odekunle and Eludoyin 2008; Ali et al. 2011; Kouadio et al. 2013). It is composed of two
 77 parts: west of Cape Three Points off Ivory Coast, and further east, off Ghana, Togo and Benin,
 78 and both parts are surrounded by the eastward Guinea Current (Odekunle and Eludoyin 2008).
 79 The dynamics of the Guinea coast upwelling remains poorly understood, however Djakouré et al.
 80 (2017) performed idealized numerical experiments and found that while the coastal upwelling
 81 west of Cape Three Points is highly sensitive to the inertia and detachment of the Guinea Current

82 from the coast, the upwelling east of Cape Three Points is primarily induced by local winds
 83 through the divergence of the Ekman transport. Ali et al. (2011) found strong correlations between
 84 GCR variability and equatorial and coastal upwellings, and Bakun (1978) observed a significant
 85 reduction in precipitation along the coast where coastal upwelling is strongest. Other studies have
 86 suggested an influence of Guinea Coast upwelling on nearby continental precipitation (Gu and
 87 Adler 2004; Kouadio et al. 2013; Nnamchi and Li 2011; Aman et al. 2018). SST in the Gulf
 88 of Guinea, particularly in the equatorial and coastal upwelling areas, could therefore influence
 89 the GCR demise as well as its onset, in particular via the modification of meridional land-sea
 90 temperature gradient as suggested by Nguyen et al. (2011b); but to our knowledge, no studies have
 yet examined the involved mechanisms.



35 FIG. 2. Scheme of the SST influence on precipitation through low-level convergence between the equator
 36 and the Guinea Coast from before T_{ref} to after T_{end} : monsoon flow (light blue horizontal arrows), low-level
 37 convergence (black upward arrows) or divergence (black downward arrows), and resulting precipitation (black
 38 hatches). May, June and July tags are not specific but rough indicators.

91 In addition to the seasonal cycle, the land-sea temperature gradient also exhibits a strong diurnal
92 cycle (Sultan et al. 2007) related to land-sea breeze regimes (Gbambie and Steyn 2013; Abayomi
93 et al. 2007; Parker et al. 2017; Guedje et al. 2019; Coulibaly et al. 2019). The land-sea breeze
94 strength is maximum in boreal winter, but a second maximum is found in May, before reaching an
95 annual minimum in July-August (Guedje et al. 2019; Coulibaly et al. 2019): its interaction with
96 the monsoon flow could therefore impact the GCR variability. In particular, land-sea breeze has
97 a strong impact on the atmospheric boundary layer at diurnal timescale, through the triggering of
98 convection (Flamant et al. 2018; Knippertz et al. 2017; Parker et al. 2017). Therefore, a thorough
99 study of the GCR needs to be done at diurnal timescales.

100 The SST influence on the GCR onset has already been investigated in previous studies over
101 the decade 2000-2009 (Leduc-Leballeur et al. 2013; Meynadier et al. 2015). The present work
102 extends this study to the whole GCR period between 2008 and 2015, and in addition, the influence
103 of the coastal upwelling on the end of the GCR is investigated. Recently available data with an
104 hourly resolution allow us to study the impact of the land-sea surface temperature gradient on
105 the precipitation at diurnal timescales. Reanalyses from the European Centre for Medium-Range
106 Weather Forecasts (ERA5) and satellite observations of clouds and precipitation are used to examine
107 the links between surface temperature, low-level atmospheric convergence and precipitation at
108 seasonal and diurnal timescales. Low-level convergence is indeed known to be strongly connected
109 with precipitation: Weller et al. (2017) found that between 65% and 90% of the precipitation is
110 associated with long coherent lines of low-level convergence over the global oceans, against 30% to
111 60% over land. It is therefore interesting to investigate if low-level convergence could be controlled
112 by the surface temperature gradients in the Gulf of Guinea, and what impact it could have on the
113 GCR, in particular on its onset and demise.

114 The first section describes the different datasets. Section 2 investigates the GCR onset and
115 confirms that previous results are found again with these new data. Section 3 investigates the GCR
116 at diurnal timescales. Section 4 presents an estimate of the GCR demise date using a surface
117 temperature index in the core of the coastal upwelling and composites computed around this date.
118 A summary and conclusion are presented in section 5.

119 2. Data and method

120 Cloud types are extracted from SAFNWC cloud type product, using an algorithm (Derrien and
121 Gléau 2005, 2010) developed for measurements of the Spinning Enhanced Visible and InfraRed
122 Imager (SEVIRI). This instrument on board the Meteosat Second Generation (MSG) is an optical
123 imaging radiometer including 12 different spectral channels in the visible and infrared range with
124 a 1-3 km spatial resolution and a 15 minutes temporal sampling. For each 3 km pixel, the cloud
125 presence (1) or absence (0) in each of the 21 different classes is indicated. From these 21 classes
126 available in the database, we merge “low” (class 6) and “ultra low clouds” (class 8) in a mixed class
127 called hereafter “low clouds”. We also gather “thick high clouds” (class 12) and “very thick high
128 clouds” (class 14) in a mixed class called “probable deep convective clouds”. To keep the data set
129 easy to use, and for comparison with others, a reduced grid mesh ($0.25^\circ \times 0.25^\circ \times 1$ hour) is used.
130 In each grid mesh the probability of occurrence of clouds in each cloud class is calculated, as well
131 as the associated spatial variance.

132 Precipitation intensity is provided by mission level 3 product 3B42V7 (TRMM) (Huffman et al.
133 2007). It has been derived primarily from the TRMM mission until 2014, and is a multi-mission
134 product (microwave and infrared radiometers), before it was recently stopped ¹. Product resolution
135 is $0.25^\circ \times 0.25^\circ$, every 3 hours. Precipitation is transformed into an event occurrence by summing
136 the events with a quantity greater than 0.1mm/h to limit the quantitative bias known to exist with
137 parameterized convection. Akinsanola et al. (2016) showed that TRMM was one of precipitation
138 datasets that can be used for precipitation assessment over West Africa.

139 ERA5 ECMWF reanalysis was generated using the four-dimensional variational analysis system
140 (C3S 2017; Hersbach et al. 2020). Data were extracted at 27 levels from 1000 to 100 hPa with a
141 0.25° horizontal resolution. The parameterization of the convection scheme has been changed since
142 the previous version of reanalyses (ERA-Interim) by adding a convective available potential energy
143 (CAPE) closure based on the work presented in Bechtold et al. (2014), which showed a better
144 representation of the diurnal cycle. Analysis variables (wind, relative humidity, temperature, total
145 column water vapor) are retrieved at a 6-hour resolution (0, 6, 12 and 18h UTC). Precipitation is
146 the addition of shallow, large-scale and convective rainfalls in forecast variables, and is retrieved at
147 a hourly time step from the +6h to +18h forecasts, twice a day. Surface fields as 10m-surface wind

¹<https://pmm.nasa.gov/data-access/downloads/TRMM>

148 and skin temperature (SKT) is also retrieved at an hourly resolution. The surface parameterization
149 scheme computes SKT in two different ways, whether on the ocean or on the continent. On
150 the ocean, the SKT product is based on a model simulation with data from satellite-derived SST
151 (Hersbach et al. 2020) which is quite close to the SKT, with a small bias of less than 0.3°C and a
152 similar variability (not shown). In spite of a significant improvement from the previous ECMWF
153 reanalysis (ERA-Interim), the continental SKT in ERA5 is still not very reliable (Johannsen et al.
154 2019), especially in southern West Africa (Flamant et al. (2018), see in particular their figure S6).
155 However, SKT (and not SST) is considered here in the coastal region of southern West Africa
156 because it makes possible to compute the surface temperature gradient between the continent and
157 the sea at diurnal timescale. The difference between SKT and SST is rather small, the SKT is
158 colder than the SST of up to 0.2° C between 1N and 3N (not shown). It is also notable that this
159 difference is minimal and almost zero, near the coast when the coastal upwelling appears in July.
160 The 10m-wind is very close from the assimilated satellite product (ASCAT during 2008-2015)
161 and is weakly biased in the region under scrutiny (see additional Figure A1). Part of the infrared
162 measurements used in TRMM precipitations are also assimilated in this reanalysis. These data
163 were provided by the Copernicus Climate Change Service and made available by the IPSL / ESPRI
164 mesocentre:

165 <https://confluence.ecmwf.int/display/CKB/ERA5%3A+data+documentation>

166 Results presented in this study are mainly based on ERA5, but three additional reanalyses are
167 also investigated:

168 - MERRA-2 : a $0.5^{\circ} \times 0.625^{\circ}$ hourly reanalysis produced by NASA's Global Modeling and
169 Assimilation Office (Gelaro et al. 2017) with version 5.12.4 of the Geostationary Operational
170 Environmental Satellites atmospheric data assimilation system. To deal with the difficulty of
171 maintaining a realistic balance between total mass and total water vapor, sources and sinks of
172 atmospheric water have been added to the model continuity equation so that changes in total mass
173 are driven by changes in total water. MERRA-2 products are accessible online through the NASA
174 Goddard Earth Sciences Data Information Services Center (GES DISC).

175 - Climate Forecast System Reanalysis (thereafter CFSR, Saha and co authors (2014) : a global,
176 high resolution, coupled atmosphere-ocean-land surface-sea ice system including coupling of

177 atmosphere and ocean during the generation of the 6 hour guess field, with an atmosphere resolution
178 of about 38 km (T382) with 64 levels.

179 - JRA-55 (thereafter JRA) is a $0.5^\circ \times 0.5^\circ$ 3-hourly atmospheric reanalysis produced by the Japan
180 Meteorological Agency (Kobayashi and coauthors 2015), with a TL319 global spectral model
181 using a conservative semi Lagrangian scheme in which vertically advection is processed separately
182 from horizontal advection (so that the model may preserve the conservation of vertically integrated
183 quantities, such as water vapor, under non-dissipative conditions).

184 The data used hereafter is 3 and 6h-forecasts based on analysis with a 6h timestep. The following
185 observational datasets of SST and surface wind are also retrieved at the daily scale:

186 - high-resolution Reynolds SST product developed using optimum interpolation, the Advanced
187 Very High Resolution Radiometer (AVHRR) infrared satellite SST data and in situ data from ships
188 and buoys (Reynolds et al. 2007), retrieved from the NOAA NCDC website ², with a spatial grid
189 resolution of 0.25° . The difference between this observed SST and the SKT ERA5 (see Figure A1)
190 shows two regions where the biases are maximum: between the equator and 2N, with a cold bias in
191 ERA5 SKT of 0.4°C in May that increases up to 0.7°C after the emergence of equatorial upwelling
192 and a second bias close to the coast, cold and rather weak in May and June (0.1°C) which become
193 a warm bias of about 0.2°C in July with the development of coastal upwelling.

194 - ASCAT ocean surface winds, or 10-meter neutral stability wind, obtained from the following
195 website: <https://manati.star.nesdis.noaa.gov/datasets/ASCATData.php>. The latter product, pro-
196 cessed by the NOAA, is derived from scatterometer measurements of Advanced SCATterometer
197 (ASCAT), aboard EUMETSAT Meteorological Operational (METOP) satellite. The geophysical
198 model function (GMF) is CMOD5.5: it relates the normalized radar cross-section to the ocean
199 surface wind speed and direction. The original grid resolution is 0.25° and data are available at
200 daily timescale.

201 The present study focuses on the southern coastal region of West Africa, extending from Ivory
202 Coast to Benin between 7W and 3E, and from May to July 2008-2015 (blue frame in Figure
203 1). Results showing vertical circulation maps or time / latitude diagrams are based on averages
204 computed between 1W and 1E, in order to accurately monitor hourly events in the diurnal cycles
205 presented in sections 3 and 4, and in section 2 for simplicity and consistency between the different

²<http://www.esrl.noaa.gov/psd/>

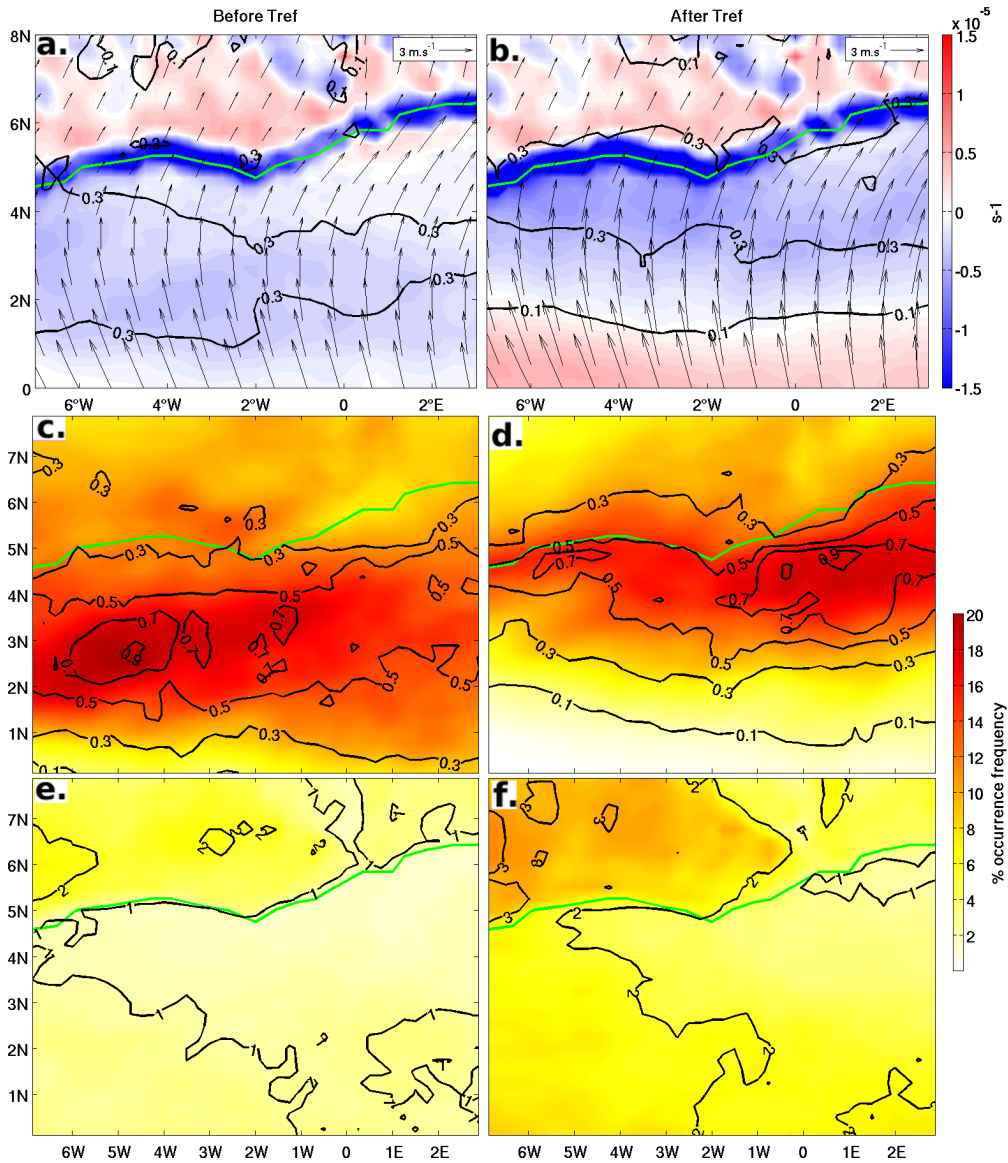
206 plots. Taking a different longitude band (5 bands of 2° , from 5W-3W to 3E-5E, were tested) only
207 slightly changed the results and left the conclusions of this study unchanged.

208 **3. Onset of the Guinea Coast Rainfall**

209 Figure 1 shows a monthly climatology of SST (color shading and black contours) and precipitation
210 (gray shading) in ERA5, from May to July between 2008 and 2015 in the Eastern Tropical Atlantic.
211 In May, a zonal band of intense precipitation extends between the Equator and the Guinea Coast,
212 with a maximum around 3N (Figure 1a). In June, the zonal band settles just south of the Guinea
213 Coast, with values greater than 8 mm/day confined north of 3-4N in the region Eq-8N, 7W-3E (blue
214 frame, Figure 1b). Between May and June, the emergence of the equatorial upwelling induces
215 a strong positive SST gradient of about $2-3^\circ\text{C}$ around its northern front (roughly at 1N), which
216 persists until July despite a general cooling of the SST : Meynadier et al. (2015) showed that this
217 front intensification forces the GCR onset by increasing the atmospheric pressure gradient across
218 the front, which strengthens the southerlies toward the Guinea Coast.

223 The Atlantic equatorial upwelling is known to exhibit very large interannual variability regarding
224 its date of emergence and intensity (Marin et al. 2009; Caniaux et al. 2011), and so is the GCR
225 (Worou et al. 2020). Moreover, precipitation data is very scattered and not normally distributed
226 (see additional Figure A2): a date of the GCR onset based on precipitation is therefore very difficult
227 to define objectively. On the other hand, previous studies have identified an abrupt change in the
228 surface wind pattern associated with the equatorial upwelling emergence, when southerlies between
229 the equator and the coast become stronger than south of the equator in the equatorial upwelling
230 (also known as the Atlantic Cold Tongue) region (Leduc-Leballeur et al. 2013; Meynadier et al.
231 2015). The date of the GCR onset, thereafter T_{ref} , is computed by following this method: it is
232 defined as the day when southerlies averaged in the box 3W-5E / 1N-4.5N (north of the front)
233 become, and remain, stronger than in the box 3W-5E / 4S-0N (south of the front) for the remaining
234 of the season. Using 2000-2009 QuikSCAT surface wind, previous studies found that T_{ref} occurred
235 after 12 May and before 25 June, with an average on 30 May (Leduc-Leballeur et al. 2013). In the
236 present study, using 2008-2015 ASCAT meridional surface wind, its range is 16 May – 6 June with
237 an average on 27 May. Note that (Sultan and Janicot 2003) estimated a date of monsoon pre-onset
238 by taking the day when the westward zonal wind averaged between 10W and 10E turns eastward

239 at 15N (i.e. going from negative to positive values): they found 14 May on average (plus or minus
 240 a root-mean-square of 9.5 days).



219 FIG. 3. Composites of 14 days before (left) and after (right) T_{ref} : a-b. ERA5 surface wind (black arrows),
 220 surface wind divergence (s^{-1} , shading) and precipitation (black contours, mm/h). c-d MSG convective clouds
 221 (shading) and TRMM precipitation (black contours, mm/h). e-f MSG low clouds (shading) and their spatial
 222 variance (black contours). Green line stands for the coastline.

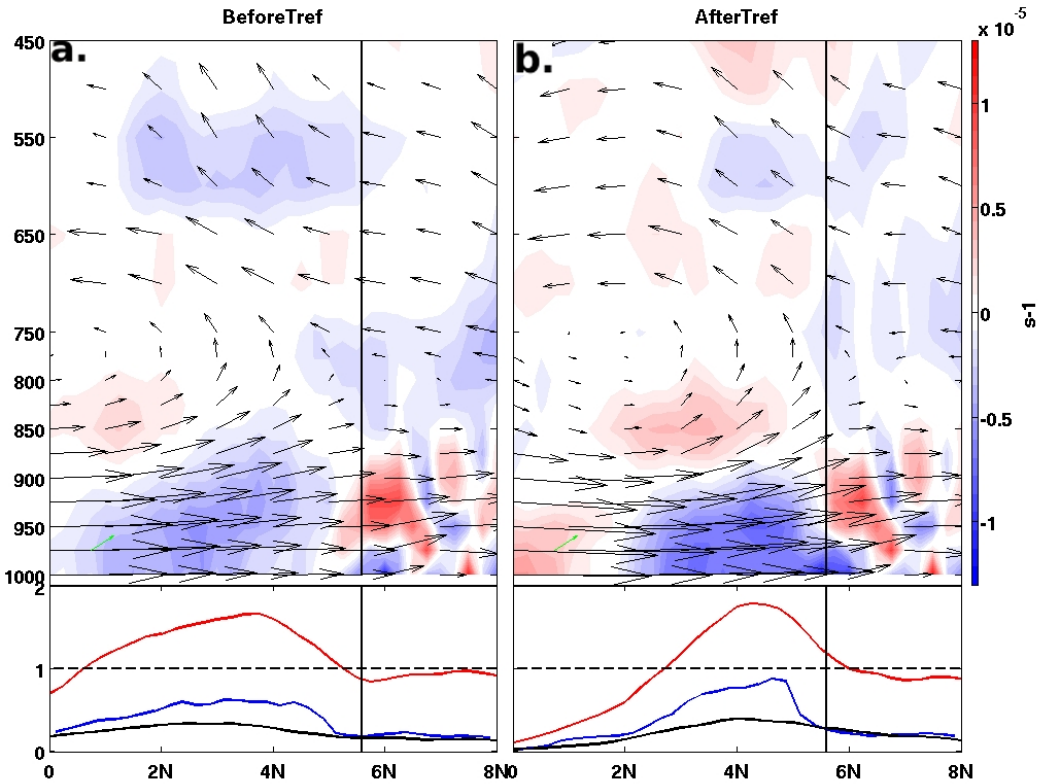
240
 241 Two composites of ERA5 surface wind divergence and MSG cloud cover were computed around
 242 T_{ref} : the first is an average over 2008-2015 of the two weeks preceding T_{ref} (i.e. between T_{ref}

243 minus 14 days and T_{ref} , Figure 3, left column), and the second of the two weeks following T_{ref}
244 (between T_{ref} and T_{ref} plus 14 days, Figure 3, right column). Weak surface convergence is found
245 throughout the Gulf of Guinea before T_{ref} , except along the Guinea Coast where surface wind is
246 strongly convergent (Figure 3a): surface wind decreases a lot when it encounters the continent,
247 mainly because of a much larger friction over the land than over the ocean which deepens the
248 boundary layer through induced turbulence. In addition, a warmer continental surface could also
249 contribute to the boundary layer deepening and weakening of surface wind over the continent, but
250 the implied surface heat flux is clearly dominated by the strong diurnal cycle of the continental
251 surface temperature, which is investigated in the next section. Convective clouds are frequent
252 (10 to 20% of the time) between the equator and the coast (at 5-6N), with a maximum around
253 2-3N (Figure 3c, shading). The precipitation is scattered over the ocean, with a maximum around
254 2-3N, in observations (Figure 3c, black contours) as well as in ERA5 (Figure 3a, black contours),
255 although they are about twice as low in the latter. Low clouds are generally scarce (less than 5%
256 of the time), with a maximum found on the continent, west of 1W (Figure 3e).

257 After T_{ref} , the surface wind strengthens in the Gulf of Guinea, mostly driven by the meridional
258 SST gradient across the northern front of the equatorial upwelling: when the latter intensifies, it
259 increases the magnitude of the atmospheric pressure gradient across the front through hydrostatic
260 balance (not shown), which strengthens surface wind from the cold to the warm side of the front
261 (Lindzen and Nigam 1987). A meridional gradient of SST therefore induces a wind divergence
262 when the gradient is positive along the mean wind direction, and a convergence when it is negative
263 (et al 2001; Chelton et al. 2004). Furthermore, previous studies showed that the warming of the sea
264 surface temperature decreases vertical atmospheric stability, thereby increasing vertical turbulent
265 flux of horizontal momentum from stronger winds aloft : this also tends to strengthen the surface
266 wind blowing from cold to warm areas within a few minutes or hours (Sweet et al. 1981; Wallace
267 et al. 1989; S.P. et al. 1989). As a result, over the cold tongue and its northern front, a strong
268 divergence of surface wind is found south of 3N after T_{ref} , which tends to inhibit deep atmospheric
269 convection and precipitation, while between 3N and the Guinea Coast an increased convergence
270 against the Guinea Coast maximizes precipitation (Figure 3b).

274 T_{ref} seasonal transition is also clearly visible in both convective clouds (Figure 3d, shading) and
275 low clouds occurrence (Figure 3f), as well as in TRMM precipitation (Figure 3d, black contours): a

276 northward shift of convective clouds toward the coast is clearly observed, with a maximal occurrence
 277 of 15 to 20% in a zonal band between 3N and 6N, in good agreement with the northward shift of
 278 convergence seen in ERA5 (Figure 3b). South of 3N, low clouds, which include both stratiform
 279 and shallow cumuliform clouds, become more frequent (Figure 3f), probably in response to the
 280 increase of surface wind divergence. Indeed, subsidence over cold areas in eastern tropical oceans
 281 enhances the temperature inversion capping the marine boundary layer, which favors the formation
 282 of low-level stratus (Myers and Norris 2013). Eventually, observed precipitation maximum is in
 283 very good agreement with the location of convective clouds (Figure 3, c-d). This good match
 confirms that the chosen cloud class is a very good proxy for monitoring deep convection.



271 FIG. 4. Composites of 14 days before (a) and after (b) T_{ref} , 1W-1E: ERA5 horizontal wind divergence
 272 (shading) and meridional circulation (black arrows), MSG convective cloud occurrence frequency ($\times 10\%$, red
 273 line) and precipitation (ERA5 in black line, TRMM in blue line, mm/h).

284
 285 Figure 4 shows composites of vertical meridional circulation in ERA5 between 1W and 1E
 286 around T_{ref} , allowing to observe the vertical extension of the divergence / convergence dipole
 287 patterns observed at the surface. Below each cross-section, precipitation in ERA5 (black) and

288 TRMM (blue), and MSG convective cloud occurrence (red) are also plotted. Before T_{ref} , the
289 strong northward Monsoon Flow is observed below 850 hPa, with an overlying southward and
290 partially convecting flow above 750 hPa (Figure 4a). This return flow subsides south of 2S, driven
291 by the South Atlantic high pressure (not seen in the figure). After T_{ref} , as discussed previously,
292 the wind is weaker south of the equator and stronger further north, inducing a surface divergence
293 and a low-level subsidence south of 2N, while surface convergence and convection have increased
294 toward the coast (Figure 4b). Precipitation in ERA5 matches this change in low-level divergence:
295 before T_{ref} , values are maximum around 2-3N (Figure 4a, black profile); after T_{ref} , they decrease
296 (increase) south (north) of 3N (Figure 4b), following the reinforcement of the low-level divergence
297 south of 3N and convergence between 3N and the Guinea Coast.

298 As expected from horizontal maps seen in Figure 3, very similar evolution from before to after
299 T_{ref} is found in observed precipitation (Figure 4, blue profiles), but with a larger decrease south
300 of 3N and a larger increase between 3N and the Guinea Coast, and with a peak of nearly 1
301 mm/h observed just south of the coast after T_{ref} . It is clear that, in spite of a huge improvement
302 of the representation of precipitation in ERA5 compared to previous reanalyses, as for example
303 documented for intraseasonal to interannual timescales in East Africa (Gleixner et al. 2020), the
304 ERA5 reanalysis represents only about half of the observed precipitation intensity between 3N and
305 the Guinea Coast. We suggest that this bias could come from a negative bias in ERA5 surface
306 southerlies compared to the observations, between the equator and the Guinea Coast (see additional
307 Figure A1): they are indeed too weak by 0.5 to 1 m/s, which may appear as a relatively small
308 difference, but which implies a convergence near the coast after T_{ref} much more important in the
309 observations than in ERA5 (compare Figures 3a-b and A3a-b), which could partly explain the too
310 scarce precipitation in ERA5 (the other possibility being obviously a flaw in the parameterization
311 of the deep atmospheric convection in ERA5, as in all global atmospheric models).

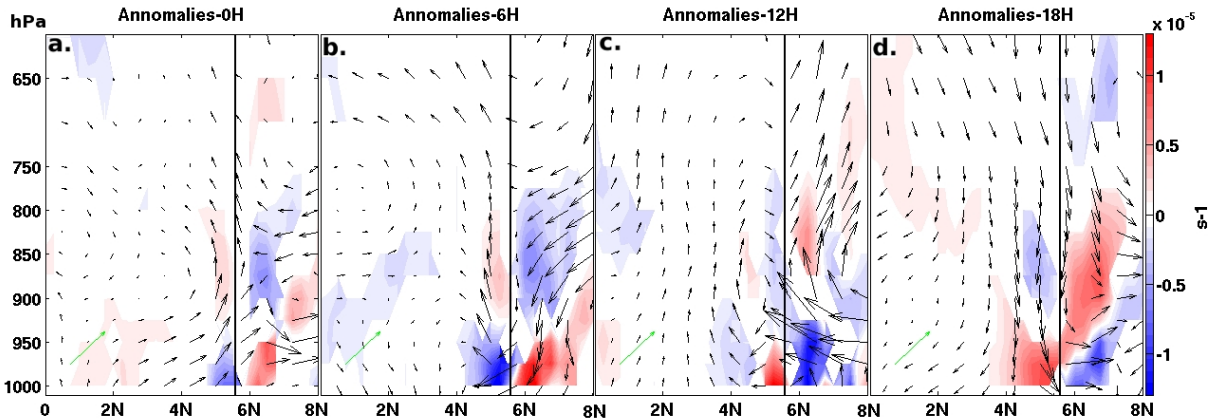
312 In summary, the dynamics of the low-level atmosphere in ERA5 corresponds to the pattern of
313 convergence of surface winds and precipitation, with divergence tending to inhibit deep convection
314 and precipitation south of 3N, and convergence tending to favor them north of 3N after T_{ref} . As
315 already explained, these changes can be attributed to changes in surface temperature, in particular
316 to the intensification of the northern front of the cold tongue (Figure 1b): following a similar
317 reasoning, the development of the coastal upwelling along the Guinea Coast in July could play a

318 role in the disappearance of the GCR (Figure 1c). But before investigating this issue, as it leads
 319 the study closer to the continent, the diurnal cycle becomes important and is first examined in the
 320 next section.

321 4. Diurnal cycle of the Guinea Coast Rainfall

325 Diurnal anomalies of the vertical meridional atmospheric circulation during the GCR sea-
 326 son are computed by subtracting the zonal / vertical wind composite averaged over the two
 327 weeks lagging T_{ref} in 2008-2015 between 1W and 1E (shown in Figure 4b) from similar
 328 composites computed at 0h, 6h, 12h or 18h (Figure 5). Note that diurnal anomalies of
 329 surface wind speed anomalies do not exceed + or - 0.5 m/s within the day on either side of
 330 the coast (not shown), against more than 3 or 4 m/s on average for the seasonal composite:
 331 the strong southern Monsoon Flow below 850 hPa is clearly larger than any diurnal wind variability.

332



322 FIG. 5. Diurnal composites of 14 days after T_{ref} , 1E-1W: ERA5 diurnal anomalies of meridional circulation
 323 (black arrows) and horizontal divergence (shading, s^{-1}) at 0h (a), 6h (b), 12h (c) and 18h (d). Green arrow stands
 324 for 1 m/s horizontally and -1 hPa/s vertically.

333 However, some diurnal anomalies of the wind divergence are found to be as large as seasonal
 334 values: for example, low-level anomalies of about $-1 \times 10^{-5} s^{-1}$ are found at 6h just south of the
 335 coast (Figure 5b), which is comparable to seasonal values in Figure 4b. The most important diurnal
 336 signal is located close to the Guinea Coast represented by a black vertical line around 5-6N, laying
 337 over about 1° (around 100 km) on both sides of the coast. This signal is in agreement with the

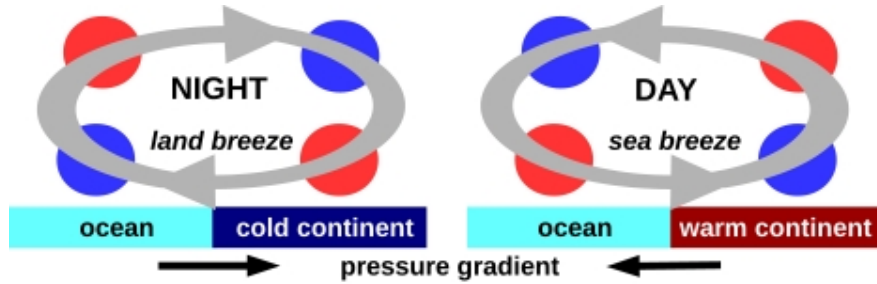
338 characteristics of a sea breeze / land breeze mechanism as described in previous studies for this
339 region (Gbambie and Steyn 2013; Parker et al. 2017; Coulibaly et al. 2019; Guedje et al. 2019).
340 Indeed, as the SST diurnal cycle is not represented in ERA5, the temperature gradient around
341 Guinea Coast closely follows the diurnal warming and cooling of the land surface (see also Figure
342 6):

343 • at 0h (Figure 5a), the land is significantly colder than the sea, which creates an anomalous
344 pressure gradient across the shore and favours a near-surface air circulation from the land toward
345 the sea (Figure 6, left), superimposed to the strong southerly Monsoon Flow. A clear meridional
346 surface wind anomaly cannot be seen yet, but the slowing down of southerlies across the coast
347 results in a more convergent surface flow to the south of the coast and divergent to the north (Figure
348 6, left). As a result, low-level convection is favoured on the ocean side, and rather inhibited on
349 the continent side. The name “land breeze” will thereafter characterize the occurrence of surface
350 wind divergence when it is convergent to the south and divergent to the north of the Guinea Coast.

351 • at 6h (Figure 5b), the land surface temperature is minimal just before sunrise, and the land breeze
352 at its most intense phase: the magnitude of the convergence / divergence dipole is maximal, with
353 a northerly surface wind anomaly and a clear convection / subduction pattern firmly established
354 across the Guinea Coast.

355 • at 12h (Figure 5c), the land has become warmer than the sea, so the land-sea anomalous pressure
356 gradient reverses and strengthens southerlies across the coastline, inducing increased divergence on
357 the sea side which inhibits convection and increased convergence on the land side which strongly
358 favours convection: it will be thereafter called "sea breeze" (Figure 6, right).

361 • at 18h (Figure 5d), a clear southerly surface wind anomaly across the coast is observed, together
362 with a strong inhibition of convection just south of the coast. In spite of near-surface convergence,
363 the convection is also inhibited on the continent side, suggesting that the sea breeze is going on but
364 may have passed its maximal daily intensity.

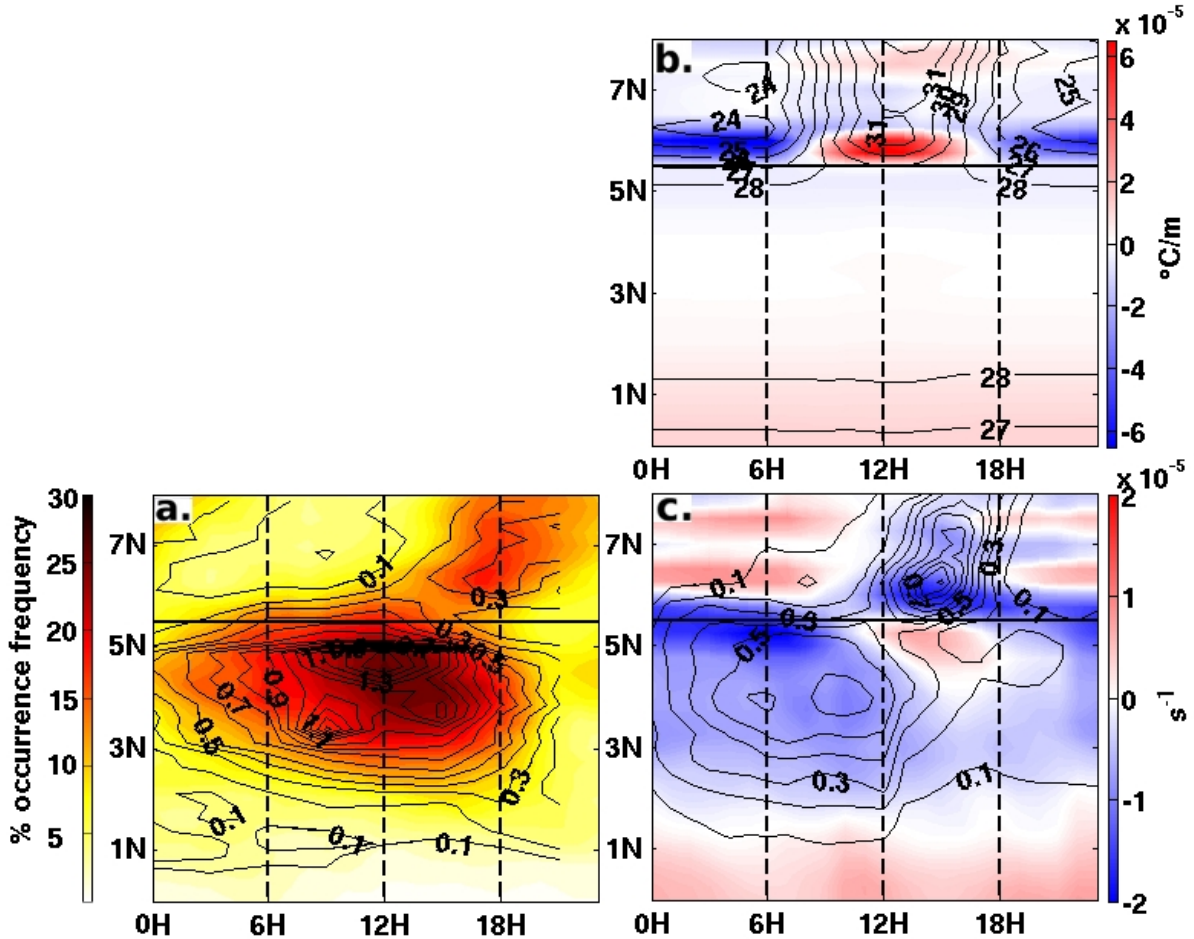


359 FIG. 6. Scheme of the land / sea breeze during night (cold continent) and day (warm continent). Red disks
 360 stand for divergence, blue ones for convergence.

365 In order to balance the sea breeze / land breeze alternation at the surface, and probably because
 366 of mass conservation within the dense Monsoon Flow (Figure 6), opposite divergent / convergent
 367 dipoles overhanging the surface ones appear between 950 and 800 hPa, especially on the land side.
 368 Their change of sign is clearly visible between 6h and 12h (Figure 5b-c).

373 Surface parameters with an hourly resolution make possible an in-depth investigation of the
 374 diurnal cycle in ERA5. SKT diurnal cycle shows a constant surface temperature of about 28°C
 375 over the ocean, while it varies over the continent between 24°C in the night and 31°C in the day
 376 (Figure 7b, black contours). A comparison between the surface temperature gradient (thereafter
 377 $dSKT/dY$, Figure 7b, shading) and the 10m-wind divergence (Figure 7c, shading) confirms that
 378 these two parameters undergo strong in-phase diurnal cycles. The “land breeze” phase is longer
 379 (around 14h) than the “sea breeze” phase (around 8h): the land breeze (negative $dSKT/dY$ in
 380 Figure 7b, and convergence south / divergence north of the coastline in Figure 7c) starts after
 381 18h in the early night and does not end before 8-9h in the following morning, with a seemingly
 382 maximum intensity around 6h just before sunrise. The sea breeze (positive $dSKT/dY$ in Figure 7b,
 383 and divergence south / convergence north of the coastline in Figure 7c) occurs during the rest of
 384 the day, i.e. between 10h and 18h, with a time lag of about 2 hours between the warmest value
 385 of $dSKT/dY$ (around 12-13h) and the maximum surface wind anomaly (around 14-15h, Figure
 386 7c). These results are in agreement with Coulibaly et al. (2019) or Gbambie and Steyn (2013),
 387 who documented the diurnal cycle with observations near the coast of Benin (located at 2°E):
 388 they similarly found that southerlies are minimum at 6h and maximum at 15h in boreal spring
 389 and summer. Surface wind therefore closely follows the diurnal pattern of land-sea temperature

390 gradient: just south (north) of the coast, it is briefly divergent (convergent) in the day and longer
 391 convergent (divergent) in the night.



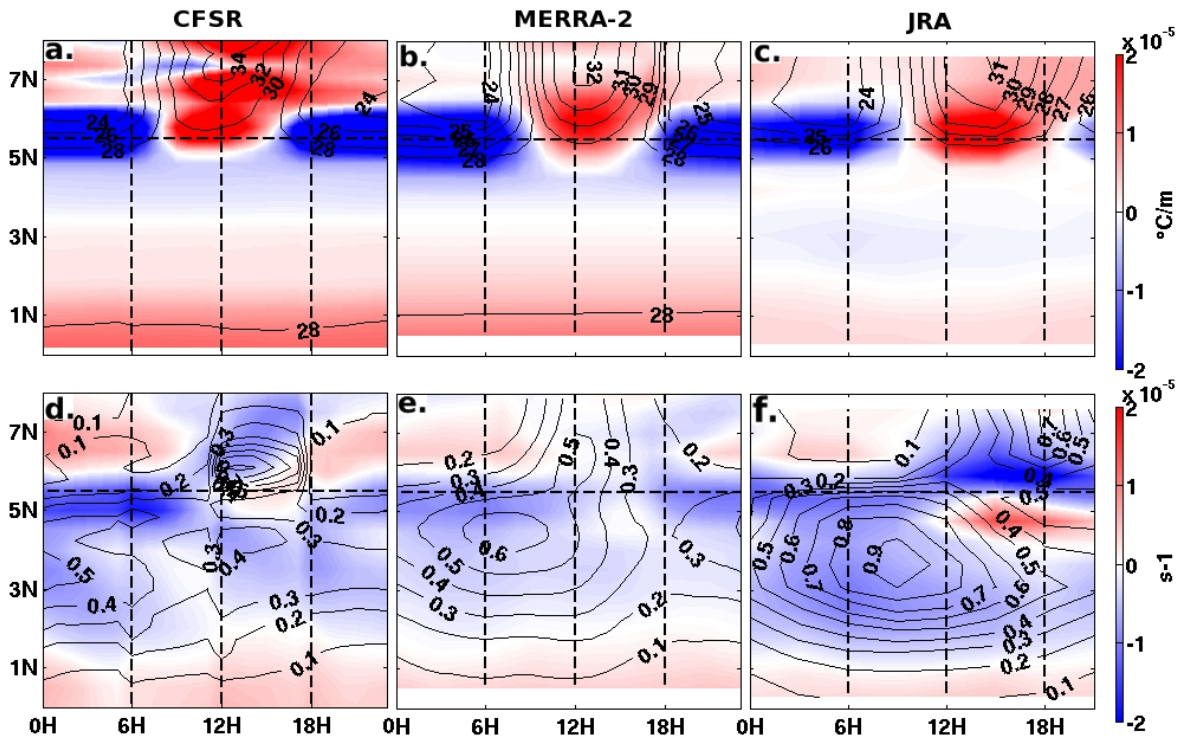
369 FIG. 7. Time-latitude diurnal composites of 14 days after T_{ref} , 1E-1W: a. MSG cloud occurrence (shading,
 370 %) and TRMM precipitation (black contours, mm/h). b. ERA5 meridional gradient of SKT (shading, $^{\circ}\text{C}/\text{m}$) and
 371 SKT (black contours, $^{\circ}\text{C}$). c. ERA5 horizontal wind divergence (shading, s^{-1}) and precipitation (black contours,
 372 mm/h). Black horizontal line stands for the mean coastline latitude.

392 A comparison is then made between ERA5 precipitation and surface divergence: along the
 393 Guinea Coast between 5N and 6N, there is a very good fit between surface wind convergence (Figure
 394 7c, shading) and precipitation (black contours): precipitation is maximum over the ocean during
 395 the night and early morning, when the land breeze convergence also reaches its maximum. Over
 396 the continent, precipitation peaks around 14-15h, at the same time as the sea breeze convergence.
 397 Conversely, divergence is associated with little or no precipitation: over the mainland north of

398 the coast during the night (land breeze, between 18h and 8h), and in the afternoon over the ocean
399 (sea breeze, 10h-18h). Note that the divergence of the sea breeze also explains the narrow gap
400 of precipitation (about 100 km long) observed just south of the Guinean coast in early afternoon.
401 Over the ocean south of 5N, precipitation peaks in ERA5 between 8h and 11h at 4N (Figure 7c).
402 It is very interesting to note that these peaks coincide with a clear surface convergence signal that
403 appears to break away from the coast in the early morning. This could be related to an offshore
404 (upstream) propagation of a density front or gravity wave generated at the coast by land breeze
405 convergence, as suggested in studies of tropical coastal regions (Yang and Slingo 2001; Love et al.
406 2011; Birch et al. 2015; Coppin and Bellon 2019): the overnight and early morning land breeze
407 phase near the coast would then explain why precipitation shows a maximum around noon over the
408 ocean. This signal appears to propagate southward for several hundred kilometers away from the
409 Guinean coast, at a speed between 10 and 20 m/s (Figure 7c) with a maximum in the late morning
410 and a minimum in the afternoon/early night, while no significant diurnal cycle can be found in
411 the surface temperature at this location. Similar distances (several hundred km) and propagation
412 speed (about 15 m/s) for the daily rainfall maximum were also observed in the observational study
413 of Yang and Slingo (2001) in similar cases. Another hypothesis to explain the diurnal cycle of
414 convection over tropical oceans is that of cloud-radiative effects, e.g., absorption of solar radiation
415 near the cloud top stabilizing the atmosphere during the day, and longwave cooling destabilizing
416 the atmosphere near the cloud top during the night Wallace (1975), but these mechanisms account
417 for a convection peak during the night and not in the early morning as here.

418 On the continent, between 10h and 18h, a convergence signal appears to extend northward for
419 100-200 km from the coast (Figure 7c). It probably favors deep atmospheric convection, with a
420 precipitation anomaly peaking around 14-15h, as noted in previous studies (Parker et al. 2017).
421 Development of Mesoscale Convective Systems and precipitation in southern West Africa is often
422 associated with wave disturbances, or African Easterly Waves, which modulate deep convection
423 and rainfall on daily timescales (Fink and Reiner 2003): they explain between 30 and 40% of the
424 convection variance in boreal summer (Mekonnen et al. 2006) and are the main contributor to
425 the West African Monsoon precipitation in summer. The low-level convergence in the afternoon
426 associated with the sea breeze would then favor the peak of precipitation observed around 15h over
427 the continent during the passage of such a disturbance.

432 These analyses were repeated with observed precipitation (TRMM) and convective cloud occur-
 433 rence (MSG). They show convective peaks similar to those found in ERA5: over the ocean in the
 434 middle of the day, and over the continent in the afternoon (Figure 7a). However, as already seen
 435 in the meridional profiles shown in Figure 4b, the precipitation in ERA5 is about half as large as
 436 in the observations. Moreover, the precipitation peaks occur about 3 hours too early in ERA5:
 437 around 13-15h instead of 18h over the continent, and around 8-11h instead of 12h over the ocean.
 438 This flaw, which is found in most global climate and numerical weather prediction models, could
 439 be due to insufficient horizontal grid resolutions or wrong representation of vertical atmospheric
 440 stability as propose by (Guichard et al. 2004).



428 FIG. 8. Time-latitude diurnal composites of 14 days after T_{ref} , 1E-1W, in CFSR (left), MERRA2 (middle)
 429 and JRA (right). Top: meridional gradient of SKT (shading, in $^{\circ}\text{K}/\text{m}$) and SKT (black contours, $^{\circ}\text{K}$). Bottom:
 430 surface wind divergence (shading, in s^{-1}) and precipitation (black contours, mm/h). Black dashed line stands for
 431 the mean coastline latitude.

441 The previous results show that on the diurnal scale, the surface temperature gradient controls
 442 the surface wind divergence, which in turn controls precipitation. This hypothesis was tested by a

443 similar analysis performed with three other reanalysis sets: CFSR, MERRA-2, and JRA (Figure
444 8). Probably because of their coarser horizontal resolutions, the diurnal anomalies of the coastal
445 dSKT/dY extend somewhat farther from the Guinean coast, but CFSR (Figure 8a) and MERRA2
446 (Figure 8b) show sign changes at 8-9am and 4-5pm, as in ERA5. In JRA (Figure 8c), the changes
447 occur instead at 10-11h and 18-19h, probably due to a different parameterization of the land surface
448 pattern. However, all three surface wind divergence models show a clear overnight and morning
449 land breeze signal near the coast, with a precipitation maximum that appears to "break away" from
450 the most intense convergent signal (Figure 8d-f). In CFSR, the oceanic precipitation peak is much
451 too low (0.4 mm/h) but at about the right time (12-18h) and at the right latitude (4N), despite visible
452 discontinuities in the data every 6h due to forecasts reset. In MERRA2, the peak is just over 0.6
453 mm/h at 4-5N, but much too early in the day (6-8h). And in JRA, it is almost 1 mm/h, but a little
454 too far south (3-4N) and too early (8-10h) compared to observations. There is no sea breeze in
455 MERRA2, but a brief neutralization of the land breeze between 12h and 18h, a relatively weak sea
456 breeze in CFSR also between 12h and 18h, and a very strong one in JRA between 12h and 0h. The
457 best representation of continental precipitation is in JRA, with a peak of precipitation around 18h,
458 as in the observations, which is probably explained by the "sea breeze" that occurs later in the day
459 than in the other reanalyses. However, the representation of diurnal oceanic precipitation in JRA is
460 not better than in ERA5 compared to the observations. This is confirmed in the next section when
461 we examine the diurnal cycle after the end of GCR. This comparison shows a robust impact of the
462 surface temperature gradient on precipitation, and justifies the use of ERA5 as the best compromise
463 to study the processes involved in the control of precipitation by surface temperature.

464 In summary, the diurnal cycle of dSKT/dY over the Guinean coast explains the diurnal cycle of
465 surface wind divergence and precipitation in ERA5 very well, and shares the main characteristics of
466 precipitation and convective clouds found in the observations (Figure 7). In particular, an onshore
467 breeze-like signal appears to favor significant precipitation over the ocean with an early morning
468 peak, and a sea breeze-like signal appears to be related to a late afternoon peak in precipitation
469 over the continent. The duration of the onshore breeze is on average much longer during the day
470 than that of the offshore breeze, which may partly explain why GCR precipitation is more abundant
471 over the ocean than over the continent (Figure 1b). The emergence of the coastal upwelling in July
472 should then reduce the nighttime land-sea temperature difference, and hence the intensity of the

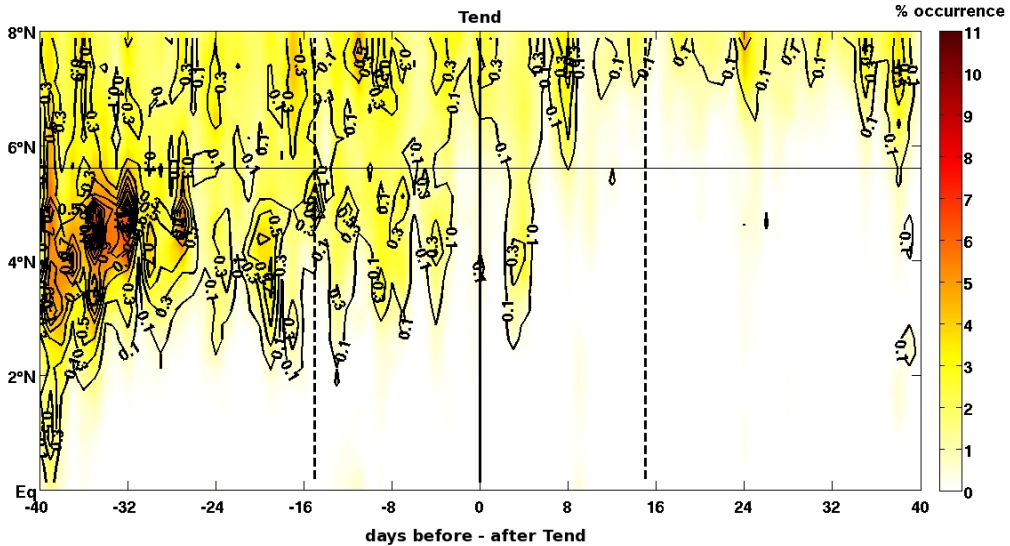
473 onshore breeze phase, and control the disappearance of coastal precipitation. This hypothesis is
474 examined in the next section using composites built around an estimate of the date of the GCR
475 demise.

476 **5. Demise of the Guinea Coast Rainfall**

477 An estimation of the date of the GCR demise was not possible using the satellite surface wind
478 as for T_{ref} , since the satellite cannot properly provides wind data within 50 km of the coast.
479 Moreover, the transition from the GCR to the little dry season is not as clear-cut as the cessation
480 of precipitation south of 3N at T_{ref} as discussed in section 2. Instead, a GCR demise date, T_{end} , is
481 computed based on the observed (Reynolds product) SST: a zone is defined between 2.5W and 3E,
482 1 to 2.5 degrees south of the coast, and an SST index is averaged in this zone from April to July,
483 2008 – 2015. An additional index (of the SST gradient) is also computed by subtracting the SST
484 at the northern edge of this area from the SST at the southern edge, in order to better characterize
485 the seasonal cooling in the coastal upwelling in late June - July, independently of the strong SST
486 interannual variability. T_{end} is then chosen as the first day when the two following criteria are true
487 until the end of July:

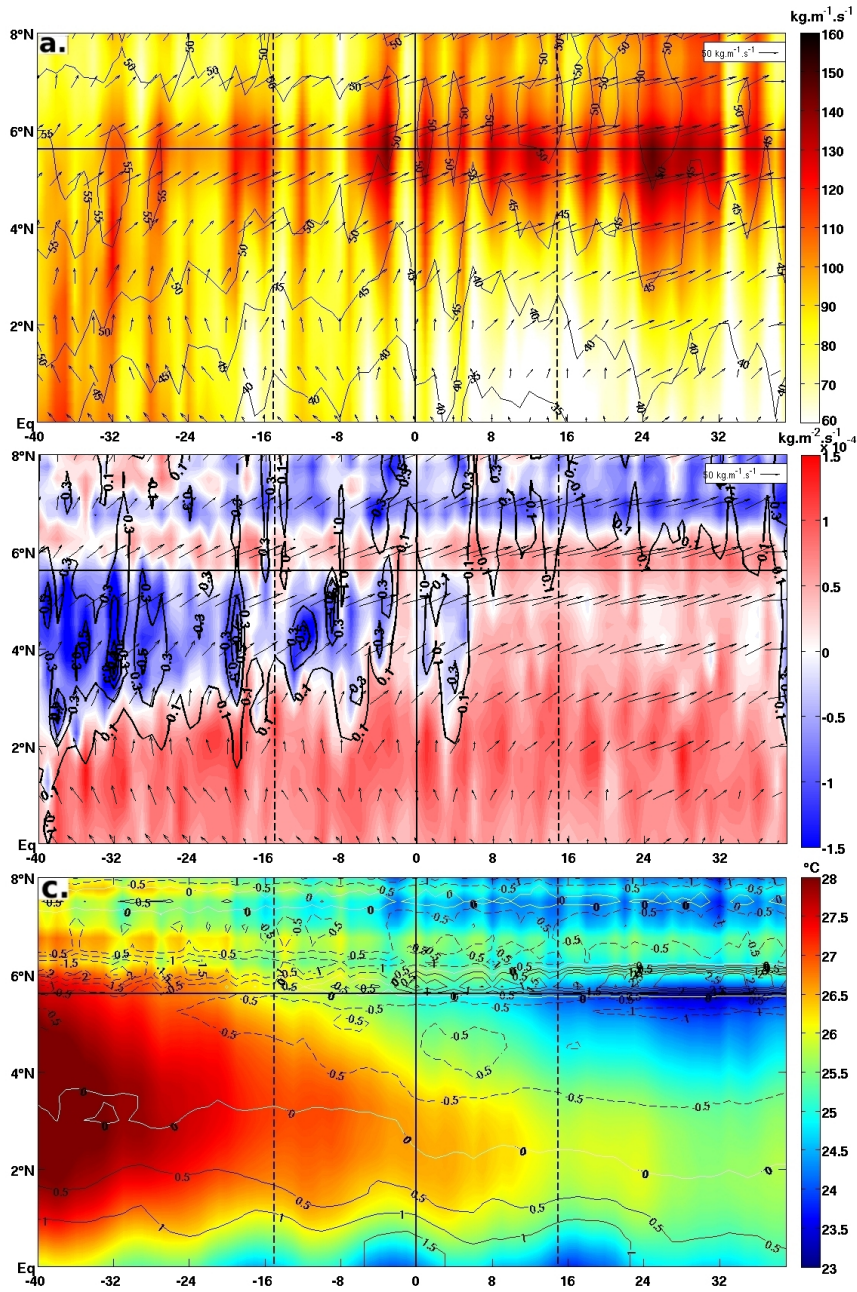
- 488 - the SST index must be lower than 80% of its values,
- 489 - the magnitude of the SST gradient index must be larger than 20% of the total magnitudes.

494 This definition is not very precise and the date typically varies by a few days by slightly modifying
495 the two criteria defined just above, however it allows us to characterize the emergence of the coastal
496 upwelling with sufficient accuracy, despite its large interannual variability : the average T_{end}
497 between 2008 and 2015 is 14 July, with values ranging from 28 June to 31 July. Note that T_{end}
498 is different from the “monsoon jump” date discussed in many previous studies (see for example
499 Fitzpatrick et al. (2015)) : the latter defines the date when the zonal band of precipitation, often
500 averaged between 10W and 10E, makes a sudden northward excursion and reaches the latitude of
501 the Sahel (Sultan and Janicot 2003), whereas the definition of T_{end} here is intended to target the
502 onset of the little dry season for the Guinea Coast countries, and these two events are apparently
503 unrelated (see additional figure A2).



490 FIG. 9. Time-latitude seasonal composites around T_{end} , 1W-1E, of convective clouds frequency (shading, in
 491 %) and TRMM precipitation (black contours, intervals of 0.2 mm/h starting at 0.1 mm/h). Vertical black line
 492 stands for lag 0 (T_{end}), dashed ones represent +/- 15 days. Black horizontal line stands for the mean coastline
 493 latitude.

504 A daily time / latitude composite built around T_{end} and averaged between 1W and 1E documents
 505 the precipitation and convective clouds during 80 days before and after T_{end} (Figure 9). A rather
 506 noisy variability remains visible at the daily timescale, but a clear seasonal trend can be noticed:
 507 the TRMM precipitation and MSG convective cloud composites show that T_{end} corresponds very
 508 well to the transition between the GCR and the little dry season, with abundant precipitation and
 509 convective clouds between 3N and 6N before T_{end} (at negative lags) and very scarce after T_{end}
 510 (positive lags); only a brief precipitation event (a little more than 0.1 mm/h) is observed 3 to 4 days
 511 after T_{end} . The little dry season is then clearly visible in this composite, with an almost complete
 512 absence of precipitation (less than 0.1 mm/h) and very few convective clouds from 8 days after
 513 T_{end} until 30 days later (Figure 9), which is consistent with the hypothesis that the emergence of the
 514 coastal upwelling partly controls the end of the GCR around mid-July on average. The involved
 515 mechanisms are then investigated in ERA5 reanalyses.



516 FIG. 10. Time-latitude seasonal composites around T_{end} , 1W-1E, in ERA5 reanalyses: a. module (shading,
 517 $\text{kg}/\text{m}\cdot\text{s}$) and direction (arrows) of the humidity transport integrated between 1000 and 850 hPa, total column
 518 water vapor (black contours, intervals of $5 \text{ kg}/\text{m}^2$). b. Humidity transport (represented by similar arrows than
 519 in a) divergence (shading, $\text{kg}/\text{m}^2/\text{s}$), and ERA5 precipitation (black contours, intervals of $0.2 \text{ mm}/\text{h}$, starting at
 520 $0.1 \text{ mm}/\text{h}$). c. SKT (shading, $^{\circ}\text{C}$) and meridional gradient of SKT (black contours, intervals of $0.5 \times 10^{-5} \text{ }^{\circ}\text{C}/\text{m}$,
 521 white contours indicate null gradient).

522 Although precipitation in ERA5 are about half that in the observations particularly during intense
523 rainfall events (the contours of precipitation peaks show several maximums around 0.5 mm/h in
524 Figure 10b, against over 1 mm/h in Figure 9), its composite shows a very good match with the
525 observations, showing a similar abrupt transition between abundant precipitation south of the
526 Guinea Coast before T_{end} and very sparse precipitation thereafter (Figure 10b, black contours).

527 Since humidity is mainly confined in the monsoon flow in the region of scrutiny, the humidity
528 transport was integrated between 1000 hPa and 850 hPa and its seasonal composite computed
529 around T_{end} . South of 3N, the northward moisture transport is quite large before T_{end} , and decreases
530 sharply after T_{end} (Figure 10a, shading), turning west / southwest. In the coastal region between
531 3-4N and 6N, it rather increases after T_{end} and clearly turns more and more eastward throughout
532 the season. The same is true for the humidity transport north of 6N, except that it increases more
533 strongly from before to after T_{end} . This is consistent with previous studies that report a significant
534 input of humidity into West Africa summer monsoon from the Eastern Atlantic, via the low-level
535 West African Westerly Jet (Pu and Cook 2012): it becomes on average larger than the humidity
536 transport from the south after the monsoon jump in summer (Lélé et al. 2015).

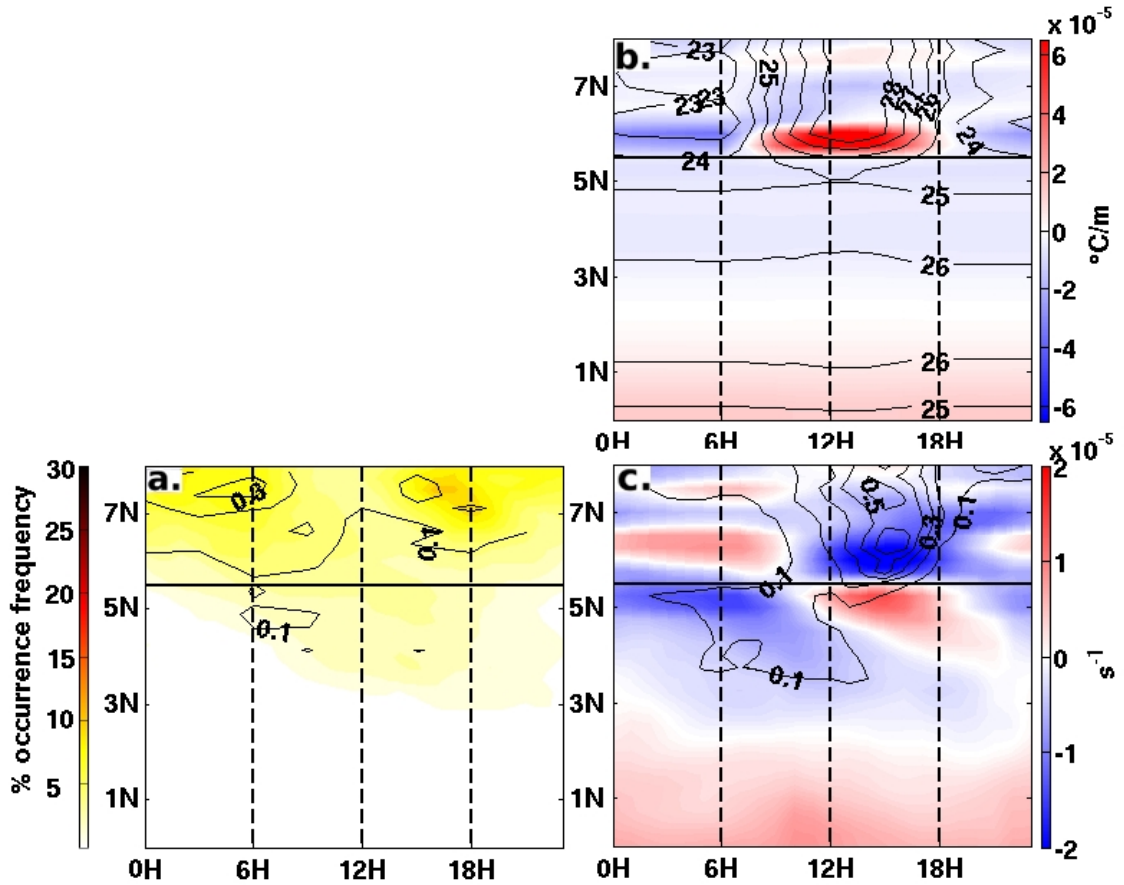
537 In agreement with the low-level humidity transport, the total column water vapor (TCWV)
538 exhibits a maximum just south of the Guinea coast before T_{end} , then this maximum slowly migrates
539 further north (Figure 10a, black contours). This migration follows the African Easterly Jet (AEJ)
540 localised around 600-700 hPa (not shown), north of the TCWV maximum, its latitude is controlled
541 by the land surface temperature and soil moisture distribution (Cook 1999) : its presence induces
542 strong vertical wind shear and horizontal vorticity, which, combined with the high TCWV value,
543 lead to the formation of mesoscale convective systems that contribute largely to the GCR. However,
544 the northward progression of the TCWV (Figure 10a, black contours) is visibly smoother than the
545 abrupt shift observed in precipitation (Figure 10b, black contours). A much better match is found
546 between precipitation and the divergence of low-level humidity transport (Figure 10b, shading),
547 which is minimum and negative (i.e. convergent) where precipitation is the largest. The seasonal
548 evolution of the humidity transport convergence can then be explained by that of the ocean surface
549 temperature, as sketched in Figure 2: between T_{ref} and T_{end} , the low-level humidity transport is
550 divergent south of 3N and convergent between 3N and the Guinea Coast (Figure 10b, negative lags),
551 forced by the emergence of the northern front of the oceanic cold tongue observed around 1-2N

552 (Figure 10c). As the coastal upwelling emerges, after T_{end} , a negative $dSKT/dY$ signal develops
553 rapidly just south of the Guinea Coast with a peak shortly after T_{end} (Figure 10c, black contours):
554 we suggest that this peak contributes to dampening the convergence of humidity transport against
555 the coast by slowing down the low-level southerlies, which would favor less oceanic precipitation
556 near the coast (see also Figure 2). Note that both mechanisms are probably involved here, the
557 negative $dSKT/dY$ forcing a positive meridional pressure gradient, as well as the SST cooling
558 increasing vertical stability in the core of the coastal upwelling. As a result, the negative $dSKT/dY$
559 signal just after T_{end} clearly corresponds to a concomitant demise of coastal oceanic precipitation.

560 Examination of the diurnal cycle provides a better understanding of this oceanic control over
561 precipitation: in the coastal region (4-7N), before T_{end} , low-level humidity transport is strongly
562 convergent over the ocean and slightly divergent over the continent (Figure 10b, negative lags until
563 -2 days), consistent with a land breeze that would be of greater amplitude than the sea breeze on a
564 daily average. After T_{end} , the decrease in humidity transport convergence over the ocean at daily
565 timescale can then be explained by a weaker land breeze phase. It is indeed what is observed in
566 the diurnal after- T_{end} composite (Figure 11c) compared to the after T_{ref} composite (Figure 7c):
567 absolute values of low-level convergence just south of the coast in the night and morning drop from
568 about $2 \times 10^{-5} s^{-1}$ after T_{ref} to about $1 \times 10^{-5} s^{-1}$ after T_{end} . And this weakening of the land breeze
569 can be explained by the decrease in the land-sea temperature difference during the night, following
570 the emergence of the coastal upwelling (Figure 11b, compared to Figure 7b).

571 However, ERA5 precipitation tends to slightly persist after T_{end} over the ocean, as it can be
572 observed in its diurnal cycle averaged on the 15 days after T_{end} : values larger than 0.1 mm/h are
573 mostly found in the morning (Figure 11c), while morning precipitation hardly reaches this value
574 in the observations (Figure 11a). In addition, too much continental precipitation, in phase with a
575 peak of sea-breeze surface convergence just north of the coast, occurs in ERA5 in the afternoon
576 (Figure 11c), whereas a rather modest convective activity is seen in the observations (Figure 11a).
577 And no continental precipitation is found in ERA5 during the night and early morning, probably
578 in response to the land-breeze divergence signal between 21h and 9h (Figure 11c), whereas a weak
579 but continuous convective activity can be tracked in the observations (Figure 11a). This suggests
580 that, although the GCR seasonal evolution is much better represented in ERA5 reanalyses than in
581 previous reanalyses, its diurnal cycle is strongly controlled by the land-sea breeze near the coast in

582 ERA5, even after T_{end} when this seems to be no longer the case in the observations. Despite these
 583 shortcomings, the results of this section clearly indicate that, by decreasing the northward transport
 584 of humidity south of the Guinea Coast and its convergence against the coast, the emergence of the
 585 coastal upwelling may well contribute to the end of the GCR and the beginning of the little dry
 586 season. In addition, this would also explain why the supply of humidity from the southern Monsoon
 587 Flow decreases in favor of that from the Eastern Atlantic via the low-level African Westerly Jet
 588 over the continent at about this time.



589 FIG. 11. Similar than in Figure 7, but for the time-latitude diurnal composites of 14 days after T_{end} instead of
 590 T_{ref} .

591 6. Summary and conclusion

592 The present study focuses on the northern Gulf of Guinea, between Benin and Ivory Coast, where
 593 observed SST data between 2008 and 2015 were used to estimate the onset (T_{ref}) and demise (T_{end})

594 dates of the Guinea Coast Rainfall (GCR), i.e. the coastal stage of the West African Monsoon,
595 in June on average, before it reaches the Sahel in summer. Composites of ERA5 reanalyses and
596 observations of precipitation and convective cloud cover are shown. The issue is to investigate
597 whether the diurnal and seasonal composites of surface temperature and oceanic or near-coastal
598 continental low-level circulation could help to understand the conditions of GCR onset and demise
599 dates.

600 The onset date, T_{ref} , was obtained by using a criteria based on low-level atmospheric dynamics,
601 which is related to the SST cooling in the equatorial upwelling region (also known as the Atlantic
602 Cold Tongue). The near-equatorial SST front strengthens the surface wind to the north and
603 weakens it to the south, as sketched in Figure 2 (middle): the low-level humidity transport becomes
604 strongly divergent south of 3N, which inhibits deep atmospheric convection and precipitation, and
605 convergent between 3N and the Guinea Coast, explaining the GCR onset.

606 This was already known from previous studies (Meynadier et al. 2015; Leduc-Leballeur et al.
607 2013), but in addition, the diurnal cycle computed with the hourly ERA5 data helped to explain
608 why the GCR precipitation mainly occurs over the ocean: oceanic precipitation starts after sunset
609 until about noon in the following day, in ERA5 as well as in observations, in very good agreement
610 with the diurnal cycle of surface wind convergence found in ERA5 just south of the coast. The
611 latter is in phase with the inversion of $dSKT/dY$ across the coast, which forces a land breeze from
612 about 19h until 11h the next day. In addition, a signal seems to detach southward from the coast in
613 late night / early morning: it could correspond to a gravity wave emitted as the land breeze is about
614 to give way to the sea breeze, and explain why a maximum is found in ERA5 precipitation as far
615 as 400-500 km from the coast during the morning / early afternoon (from noon to late afternoon in
616 the observations). Similar results were found with three other reanalysis ensembles, although their
617 representation of the diurnal cycle is not as good as in ERA5. Despite an early shift of the diurnal
618 cycle, probably due to problems in modeling surface temperature cycle, this confirms that the
619 diurnal cycle of the coastal $dSKT/dY$ does drive the diurnal cycle of the surface wind convergence
620 near the coast.

621 As suggested by previous studies, the coastal upwelling that emerges in July along the Guinea
622 Coast has a strong impact on the disappearance of the GCR and the onset of the little dry season.
623 SST and SST gradient indices in the core of the coastal upwelling, calculated from observations,

624 were used to estimate a date of emergence of the coastal upwelling, T_{end} : with an accuracy of a
625 few days, this date is preceded by a slow decrease of the GCR, and coincides with its rather abrupt
626 disappearance, both in ERA5 and observations. In ERA5, the decrease in oceanic precipitation
627 is clearly explained by the decrease in convergence of the low-level humidity transport just south
628 of the Guinea coast, which slowly decreases before T_{end} and disappears soon after. Just south of
629 the coast, a strong meridional - negative - SST gradient is found when the upwelling emerges:
630 by decreasing the southerlies near the coast, it counteracts the effect of the positive SST gradient
631 north of the cold tongue front which intensifies them. This can clearly explain the decrease in
632 near-coastal convergence of low-level humidity and precipitation (Figure 2, bottom). Moreover, on
633 the diurnal scale, a weaker land breeze after T_{end} , due to a lower land-sea temperature difference
634 during the night because of the emergence of the coastal upwelling, also contributes to the decrease
635 in near-coastal convergence and the GCR demise.

636 These assumptions are based on seasonal composites calculated over only eight years, and
637 obviously require further investigation. If the impact of coastal upwelling on the disappearance of
638 the GCR in July were to be confirmed, it would be of major importance to determine more precisely
639 the mechanisms of this impact, and to verify that it is well represented in the weather forecasting
640 models. Indeed, the large-scale surface wind probably controls a large part of the fluctuations
641 of the coastal upwelling on synoptic and intraseasonal scales: a feedback of this upwelling on
642 the regional atmospheric circulation could have a great importance on the seasonal evolution of
643 precipitation, its intraseasonal variability, and its seasonal predictability. A poor representation of
644 this feedback could, for example, partly explain why the end of coastal precipitation is generally
645 poorly represented in climate models.

646 One element that may be important in this feedback and has not been discussed here is the low-
647 level cloud cover: it is a key element controlling the land-sea breeze in the surface energy balance,
648 and has been investigated in several studies (Knippertz et al. 2011). The intensive measurement
649 campaign of the European project Dynamics-Aerosol-Chemistry-Cloud Interactions in West Africa
650 (DACCIWA) in June-July 2016 provided important in-situ data documenting the land-sea breeze
651 in Ghana, Togo and Benin, and the interaction between low-level clouds and the emission of
652 aerosol pollutants by megacities such as Lome in Togo or Lagos in Nigeria (Knippertz et al. 2017).
653 These data could help to perform a full validation and estimation of the ERA5 reanalyses. We

654 therefore intend to extend the present study to the representation of the processes involved in coastal
655 precipitation at intraseasonal timescales in ERA5 reanalyses. In addition, numerical simulations,
656 for example with a regional atmospheric model forced by coastal upwellings of varying intensities,
657 should also allow us to estimate the importance of coastal upwelling by isolating its impact. Finally,
658 a similar study is needed for the second coastal precipitation season: the southward migration of
659 precipitation to the ocean in September-November is much smoother than the northward migration
660 in summer studied in this paper, which could also help to better understand the mechanisms involved
661 here.

662 *Acknowledgments.* We would like to thank anonymous reviewers for their comments, which were of
663 great help in improving the manuscript, and Geneviève Seze in her help to use the SEVIRI cloud
664 products. Funding: Manuel Tanguy has a PhD fellowship from UVSQ.

665 *Data availability statement.* This study benefits from SEVIRI cloud products produced and
666 distributed by AERIS / ICARE Data and Services Center, and for which we would like to thank
667 Geneviève SEZE, ERA-5 reanalyses from Copernicus Climate Change Service, available from the
668 IPSL/ ESPRI mesocentre. We also thank the NOAA / NCDC for Reynolds SST product and NOAA
669 for ASCAT wind product used, and the Institut Pierre-Simon Laplace and LATMOS for server and
670 data storage (Climserv and Ciclad).

671 Availability of data and material (data transparency): all sources of data have been mentioned
672 and are in free access.

673 Code availability (software application or custom code): yes, on demand.

674 Conflicts of interest / Competing interests (include appropriate disclosures): none

675 **References**

- 676 Abayomi, A. A., B. J. Abiodun, and B. J. Omotosho, 2007: An observational study of sea breeze
677 over nigerian coastal region. *Research Journal of Applied Sciences*, **2**, 745–751.
- 678 Adejuwon, J. O., and T. O. Odekunle, 2006: Variability and the severity of the “little dry season in
679 southwestern nigeria. *Journal of Climate*, <https://doi.org/10.1175/JCLI3642.1>.
- 680 Akinsanola, A. A., K. I. Ogunjobi, V. O. Ajayi, E. A. Adefisan, J. A. Omotosho, and S. Sanogo,
681 2016: Comparison of five gridded precipitation products at climatological scales over west
682 africa. *Meteorol. Atmos. Phys.*, <https://doi.org/10.1007/s00703-016-0493-6>.
- 683 Ali, K., K. Y. Kouadio, E.-P. Zahiri, A. Aman, A. Assamoi, and B. Bourles, 2011: Influence of the
684 gulf of guinea coastal and equatorial upwellings on the precipitations along its northern coasts
685 during the boreal summer period. *Asian Journal of Applied Sciences*.
- 686 Aman, A., E. Toualy, and F. Yoroba, 2018: On the causes of the minor dry season over the
687 coastal region of the northern gulf of guinea. *Atmospheric and Climate Sciences*, <https://doi.org/121-133>.doi:10.4236/acs.2018.82009.
- 688
- 689 Bakun, A., 1978: Guinea current upwelling. *Nature*, [https://doi.org/https://doi.org/10.1038/](https://doi.org/https://doi.org/10.1038/271147a0)
690 [271147a0](https://doi.org/https://doi.org/10.1038/271147a0).
- 691 Bechtold, P., S. N., P. Lopez, J. Chaboureau, A. Beljaars, and B. N., 2014: Representing equilibrium
692 and nonequilibrium convection in large-scale models. *Journal of the Atmospheric Sciences*.
- 693 Birch, C., M. J. Roberts, L. Garcia-Carreras, D. Ackerley, M. J. Reeder, A. P. Lock, and
694 R. Schiemann, 2015: Sea-breeze dynamics and convection initiation: The influence of con-
695 vective parameterization in weather and climate model biases. *J. Climate*, [https://doi.org/](https://doi.org/https://doi.org/10.1175/JCLI-D-14-00850.1)
696 [https://doi.org/10.1175/JCLI-D-14-00850.1](https://doi.org/https://doi.org/10.1175/JCLI-D-14-00850.1).
- 697 Bony, S., S. B., and F. D. et al, 2015: Clouds, circulation and climate sensitivity. *Nature Geoscience*,
698 **8**, <https://doi.org/https://doi.org/10.1038/ngeo2398>.
- 699 C3S, 2017: Era5 : Fifth generation of ecmwf atmospheric reanalyses of the global climate.
700 *Copernicus Climate Change Service*.

701 Caniaux, G., H. Giordani, J.-L. Redelsperger, F. Guichard, E. Key, and M. Wade, 2011: Coupling
702 between the atlantic cold tongue and the west african monsoon in boreal spring and summer. *J.*
703 *Geophys. Res.*, <https://doi.org/doi:10.1029/2010JC006570>.

704 Chelton, D., M. G. Schlax, M. H. Freilich, and R. F. Milliff, 2004: Satellite measurements reveal
705 persistent small-scale features in ocean winds. *Science*.

706 Cook, K., 1999: Generation of the african easterly jet and its role in determining west african
707 precipitation. *J. of Clim.*

708 Coppin, D., and G. Bellon, 2019: Physical mechanisms controlling the offshore propagation of
709 convection in the tropics: 2. influence of topography. *Journal of Advances in Modeling Earth*
710 *Systems*, <https://doi.org/https://doi.org/10.1029/2019MS001794>.

711 Coulibaly, A., B. J. Omotosho, and M. B. S. et al., 2019: Characteristics of land and sea breezes
712 along the guinea coast of west africa. *Theor. Appl. Climatol.*, [https://doi.org/https://doi.org/10.](https://doi.org/https://doi.org/10.1007/s00704-019-02882-0)
713 [1007/s00704-019-02882-0](https://doi.org/https://doi.org/10.1007/s00704-019-02882-0).

714 Crespo, L., N. Keenlyside, and S. Koseki, 2019: The role of sea surface temperature in the
715 atmospheric seasonal cycle of the equatorial atlantic. *Clim. Dyn.*, [https://doi.org/https://doi.org/](https://doi.org/https://doi.org/10.1007/s00382-018-4489-4)
716 [10.1007/s00382-018-4489-4](https://doi.org/https://doi.org/10.1007/s00382-018-4489-4).

717 Derrien, M., and H. L. Gléau, 2005: Msg / seviri cloud mask and type from safnwc. *International*
718 *Journal of Remote Sensing*, <https://doi.org/10.1080/01431160500166128>.

719 Derrien, M., and H. L. Gléau, 2010: Improvement of cloud detection near sunrise and sunset
720 by temporal-differencing and region-growing techniques with real-time seviri. *International*
721 *Journal of Remote Sensing*, <https://doi.org/DOI:10.1080/01431160902926632>.

722 Djakouré, S., P. Penven, B. Bourlès, V. Koné, and J. Veitch, 2017: Respective roles of the
723 guinea current and local winds on the coastal upwelling in the northern gulf of guinea. *J. Phys.*
724 *Oceanogr.*, <https://doi.org/https://doi.org/10.1175/JPO-D-16-0126.1>.

725 et al, D. C., 2001: Observations of coupling between surface wind stress and sea surface
726 temperature in the eastern tropical pacific. *J. Climate*, [https://doi.org/https://doi.org/10.1175/](https://doi.org/https://doi.org/10.1175/1520-0442(2001)014<1479:OOCBSW>2.0.CO;2)
727 [1520-0442\(2001\)014<1479:OOCBSW>2.0.CO;2](https://doi.org/https://doi.org/10.1175/1520-0442(2001)014<1479:OOCBSW>2.0.CO;2).

- 728 Fink, A., and A. Reiner, 2003: Spatiotemporal variability of the relation between african easterly
729 waves and west african squall lines in 1998 and 1999. *J. Geophys. Res.*, [https://doi.org/doi:
730 10.1029/2002JD002816](https://doi.org/doi:10.1029/2002JD002816).
- 731 Fink, A., and Coauthors, 2017: Mean climate and seasonal cycle. *Meteorology of Tropical West
732 Africa*, John Wiley and Sons, Ltd, <https://doi.org/https://doi.org/10.1002/9781118391297.ch1>.
- 733 Fitzpatrick, R., C. L. Bain, P. Knippertz, J. H. Marsham, and D. Parker, 2015: The west african
734 monsoon onset : A concise comparison of definitions. *J. Climate*, [https://doi.org/https://doi.org/
735 10.1175/JCLI-D-15-0265.1](https://doi.org/https://doi.org/10.1175/JCLI-D-15-0265.1).
- 736 Flamant, C., and Coauthors, 2018: Aerosol distribution in the northern gulf of guinea : lo-
737 cal anthropogenic sources, long-range transport, and the role of coastal shallow circulations.
738 *Atmospheric Chemistry and Physics, European Geosciences Union*.
- 739 Gbambie, A. S. B., and D. Steyn, 2013: Sea breezes at cotonou and their interaction with the west
740 african monsoon. *Int. J. Climatol*.
- 741 Gelaro, R., and Coauthors, 2017: The modern-era retrospective analysis for research and applica-
742 tions, version 2 (merra-2). *Journal of Climate*, <https://doi.org/10.1175/JCLI-D-16-0758.1>.
- 743 Giannini, Alessandra, R. Saravanan, and P. Chang., 2003: Oceanic forcing of sahel rainfall on
744 interannual to interdecadal time scales. *Science*, <https://doi.org/DOI:10.1126/science.1089357>.
- 745 Gleixner, S., T. Demissie, and G. T. Diro, 2020: Did era5 improve temperature and precipitation
746 reanalysis over east africa? *Atmosphere*, **11**, <https://doi.org/10.3390/atmos11090996>.
- 747 Gu, G., and R. F. Adler, 2004: Seasonal evolution and variability associated with the west
748 african monsoon system. *J. Climate*, [https://doi.org/https://doi.org/10.1175/1520-0442\(2004\)
749 017<3364:SEAVAW>2.0.CO;2](https://doi.org/https://doi.org/10.1175/1520-0442(2004)017<3364:SEAVAW>2.0.CO;2).
- 750 Guedje, G., A. V. V. Houeto, E. B. Houngrinou, A. H. Fink, and P. Knippertz, 2019: Climatology
751 of coastal wind regimes in benin. *Meteorol. Z. (Contrib. Atm. Sci.)*.
- 752 Guichard, F., and Coauthors, 2004: Modelling the diurnal-cycle of deep precipitating convection
753 over land with cloud-resolving models and single-column models. *QRMS*.

- 754 Hagos, S. M., and K. H. Cook, 2007: Dynamics of the west african monsoon jump. *J. Climate*,
755 <https://doi.org/https://doi.org/10.1175/2007JCLI1533.1>.
- 756 Harlaß, J., M. Latif, and W. Park, 2015: Improving climate model simulation of tropical atlantic
757 sea surface temperature: The importance of enhanced vertical atmosphere model resolution.
758 *Geophys. Res. Lett.*, **42**, <https://doi.org/10.1002/2015GL063310>.
- 759 Hersbach, H., B. Bell, and P. B. et al., 2020: The era5 global reanalysis. *Q J R Meteorol Soc.*,
760 <https://doi.org/https://doi.org/10.1002/qj.3803>.
- 761 Huffman, G., and Coauthors, 2007: The trmm multisatellite precipitation analysis (tmpa): Quasi-
762 global, multiyear, combined-sensor precipitation estimates at fine scales. *J. Hydrometeorol.*
- 763 Johannsen, F., S. Ermida, J. Martins, P. Trigo, F. Isabel, M. Nogueira, and E. Dutra, 2019: Cold bias
764 of era5 summertime daily maximum land surface temperature over iberian peninsula. *Remote*
765 *Sensing*.
- 766 Kniffka, A., and Coauthors, 2020: An evaluation of operational and research weather forecasts
767 for southern west africa using observations from the dacciwa field campaign in june–july 2016.
768 *Quarterly Journal of the Royal Meteorological Society*, **146 (728)**, 1121–1148, [https://doi.org/](https://doi.org/https://doi.org/10.1002/qj.3729)
769 <https://doi.org/10.1002/qj.3729>.
- 770 Knippertz, P., A. Fink, R. Schuster, J. Trentmann, J. Schrage, and C. Yorke, 2011: Ultra-low
771 clouds over the southern west african monsoon region. *Geophys. Res. Lett.*, [https://doi.org/](https://doi.org/doi:10.1029/2011GL049278)
772 [doi:10.1029/2011GL049278](https://doi.org/doi:10.1029/2011GL049278).
- 773 Knippertz, P., and Coauthors, 2017: A meteorological and chemical overview of the dacciwa
774 field campaign in west africa in june–july 2016. *Atmos. Chem. Phys.*, [https://doi.org/https://doi.org/https://doi.org/10.5194/acp-17-10893-2017](https://doi.org/https://doi.org/10.5194/acp-17-10893-2017).
- 775 <https://doi.org/https://doi.org/10.5194/acp-17-10893-2017>.
- 776 Kobayashi, S., and coauthors, 2015: The jra-55 reanalysis: General specifications and basic
777 characteristics. *Journal of the Meteorological Society of Japan. Ser. II*, [https://doi.org/https://doi.org/https://doi.org/10.2151/jmsj.2015-001](https://doi.org/https://doi.org/10.2151/jmsj.2015-001).
- 778 <https://doi.org/https://doi.org/10.2151/jmsj.2015-001>.
- 779 Kouadio, K., S. Bastin, A. Konare, and V. Ajayi, 2018: Does convection-permitting simulate better
780 rainfall distribution and extreme over guinean coast and surroundings? *Climate Dynamics*, **55**,
781 <https://doi.org/DOI:10.1007/s00382-018-4308-y>.

- 782 Kouadio, K., S. Djakouré, A. Aman, K. E. Ali, V. Koné, and E. Toualy, 2013: Characterization of
783 the boreal summer upwelling at the northern coast of the gulf of guinea based on the propao in
784 situ measurements network and satellite data. *Int. J. of Oceanography*.
- 785 Leduc-Leballeur, M., G. de Coëtlogon, and L. Eymard, 2013: Air–sea interaction in the gulf of
786 guinea at intraseasonal time-scales: wind bursts and coastal precipitation in boreal spring. *Q.J.R.*
787 *Meteorol. Soc.*, <https://doi.org/doi:10.1002/qj.1981>.
- 788 Lindzen, R., and S. Nigam, 1987: On the role of sea surface temperature gradients in forcing low-
789 level winds and convergence in the tropics. *Journal of the Atmospheric Sciences*, [https://doi.org/
790 doi:10.1175/1520-0469\(1987\)044<2418:otross>2.0.co;2](https://doi.org/doi:10.1175/1520-0469(1987)044<2418:otross>2.0.co;2).
- 791 Losada, T., B. Rodríguez-Fonseca, and S. J. et al., 2010: A multi-model approach to the atlantic
792 equatorial mode: impact on the west african monsoon. *Clim Dyn*, **35**, [https://doi.org/https:
793 //doi.org/10.1007/s00382-009-0625-5](https://doi.org/https://doi.org/10.1007/s00382-009-0625-5).
- 794 Love, B., A. Matthews, and G. Lister, 2011: The diurnal cycle of precipitation over the maritime
795 continent in a high-resolution atmospheric model. *Q. J. R. Meteorol.*, [https://doi.org/DOI:10.
796 1002/qj.809](https://doi.org/DOI:10.1002/qj.809).
- 797 Lélé, I., L. Leslie, and P. Lamb, 2015: Analysis of low-level atmospheric moisture transport associ-
798 ated with the west african monsoon. *J. of Clim.*, <https://doi.org/doi:10.1175/JCLI-D-14-00746.1>.
- 799 Maranan, M., A. Fink, and P. Knippertz, 2018: Rainfall types over southern west africa: Objective
800 identification, climatology and synoptic environment. *Q J R Meteorol. Soc.*, **144**, [https://doi.org/
801 https://doi.org/10.1002/qj.3345](https://doi.org/https://doi.org/10.1002/qj.3345).
- 802 Marin, F., G. Caniaux, H. Giordani, B. Bourlès, Y. Gouriou, and E. Key, 2009: Why were sea
803 surface temperatures so different in the eastern equatorial atlantic in june 2005 and 2006?
804 *Journal of Physical Oceanography*, <https://doi.org/https://doi.org/10.1175/2008JPO4030.1>.
- 805 Mekonnen, A., C. D. Thorncroft, and A. R. Aiyyer, 2006: Analysis of convection and its association
806 with african easterly waves. *Journal of Climate*, <https://doi.org/10.1175/JCLI3920.1>".
- 807 Meynadier, R., G. de Coëtlogon, M. Leduc-Leballeur, L. Eymard, and S. Janicot, 2015: Sea-
808 sonal influence of the sea surface temperature on the low atmospheric circulation and pre-

809 cipitation in the eastern equatorial atlantic. *Climate Dynamics*, <https://doi.org/doi:10.1007/s00382-015-2892-7>.

810

811 Myers, T., and J. R. Norris, 2013: Observational evidence that enhanced subsidence reduces
812 subtropical marine boundary layer cloudiness. *Journal of Climate*, <https://doi.org/doi:10.1175/jcli-d-12-00736.1>.

813

814 Nguyen, H., C. D. Thorncroft, and C. Zhang, 2011a: Guinean coastal rainfall of the west african
815 monsoon. *Quarterly Journal of the Royal Meteorological Society*, **137(660)**, <https://doi.org/doi:10.1002/qj.867>.

816

817 Nguyen, H., C. Zhang, and P. Peyrillé, 2011b: Annual cycle of the west african monsoon:
818 regional circulations and associated water vapour transport. *Quarterly Journal of the Royal
819 Meteorological Society*, <https://doi.org/doi:10.1002/qj.728>.

820

821 Nnamchi, H., and J. Li, 2011: Influence of the south atlantic ocean dipole on west african summer
822 precipitation. *J. Climate*, **24**, <https://doi.org/https://doi.org/10.1175/2010JCLI3668.1>.

823

824 Odekunle, T., and A. Eludoyin, 2008: Sea surface temperature patterns in the gulf of guinea: Their
825 implications for the spatio-temporal variability of precipitation in west africa. *Int. J. Climatol.*,
826 **28**.

827

828 Okumura, Y., and S.-P. Xie, 2004: Interaction of the atlantic equatorial cold tongue and the african
829 monsoon. *Journal of Climate*, [https://doi.org/10.1175/1520-0442\(2004\)017<3589:IOTAEC>2.0.CO;2](https://doi.org/10.1175/1520-0442(2004)017<3589:IOTAEC>2.0.CO;2).

830

831 Parker, D., and Coauthors, 2017: Local weather. *Meteorology of Tropical West Africa, the Fore-
832 caster's Handbook*, Wiley Blackwell, <https://doi.org/doi:10.1002/9781118391297.ch4>.

833

834 Peyrillé, P., J. P. Lafore, and J. L. Redelsperger, 2007: An idealized two-dimensional framework
835 to study the west african monsoon. part 1: Validation and key controlling factors. *J. Atmos.Sci.*,
64, <https://doi.org/doi:10.1175/JAS3919.1>.

836

837 Polo, I., B. Rodríguez-Fonseca, T. Losada, and J. García-Serrano, 2008: Tropical atlantic variability
838 modes (1979–2002). part i: Time-evolving sst modes related to west african rainfall. *Journal of
839 Climate*, <https://doi.org/10.1175/2008JCLI2607.1>.

836 Redelsperger, J., C. Thorncroft, A. Diedhiou, T. Lebel, D. Parker, and J. Polcher, 2006: African
837 monsoon multidisciplinary analysis: An international research project and field campaign. *Bull.*
838 *Amer. Meteor. Soc.*, **87**, <https://doi.org/https://doi.org/10.1175/BAMS-87-12-1739>.

839 Roehrig, R., D. Bouniol, F. Guichard, F. Hourdin, and J. L. Redelsperger, 2013: The present and
840 future of the west african monsoon: A process-oriented assessment of cmip5 simulations along
841 the amma transect. *J. Climate*, **26**, <https://doi.org/https://doi.org/10.1175/JCLI-D-12-00505.1>.

842 Saha, S., and co authors, 2014: The ncep climate forecast system version 2. *J. Climate*.

843 Sow, M., M. Diakhaté, R. Dixon, F. Guichard, D. Dieng, and A. Gaye, 2020: Uncertainties in the
844 annual cycle of rainfall characteristics over west africa in cmip5 models. *Atmosphere*.

845 S.P., H., M. McPhaden, and J. Wallace, 1989: The influence of sea-surface temperature on surface
846 wind in the eastern equatorial pacific: Weekly to monthly variability. *J. Climate*.

847 Steinig, S., J. Harlaß, and W. P. et al., 2018: Sahel rainfall strength and onset improvements due to
848 more realistic atlantic cold tongue development in a climate model. *Sci Rep*, **8**, [https://doi.org/](https://doi.org/https://doi.org/10.1038/s41598-018-20904-1)
849 <https://doi.org/10.1038/s41598-018-20904-1>.

850 Sultan, B., and S. Janicot, 2003: The west african monsoon dynamics. part ii: The “preonset” and
851 “onset” of the summer monsoon. *J. Climate*, **16**.

852 Sultan, B., S. Janicot, and P. Drobinski, 2007: Characterization of the diurnal cycle of the west
853 african monsoon around the monsoon onset. *Journal of Climate*, **20**, [https://doi.org/10.1175/](https://doi.org/10.1175/JCLI4218.1)
854 [JCLI4218.1](https://doi.org/10.1175/JCLI4218.1).

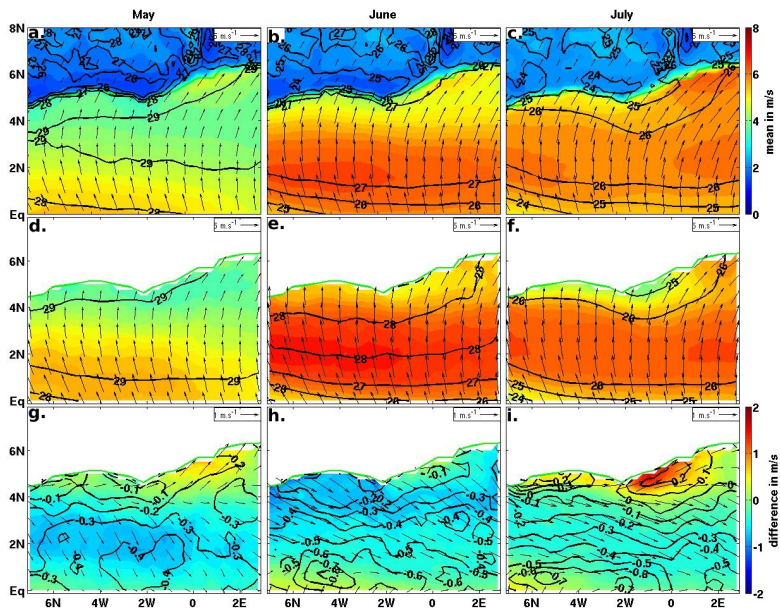
855 Suárez-Moreno, R., B. Rodríguez-Fonseca, J. A. Barroso, and A. H. Fink, 2018: Interdecadal
856 changes in the leading ocean forcing of sahelian rainfall interannual variability: Atmospheric
857 dynamics and role of multidecadal sst background. *Journal of Climate*.

858 Sweet, W., R. Fett, J. Kerling, and P. LaViolette, 1981: Air–sea interaction effects in the lower
859 troposphere across the northwall of the gulf stream. *Mon. Wea. Rev.*

860 Sylla, M., B. I. Diallo, and J. S. Pal, 2013: West african monsoon in state-of-the-science regional
861 climate models. *Climate Variability - Regional and Thematic Patterns*, [https://doi.org/doi:10.](https://doi.org/doi:10.5772/55140)
862 [5772/55140](https://doi.org/doi:10.5772/55140)Âă.

- 863 Thorncroft, C., H. Nguyen, C. Zhang, and P. Peyrill , 2011: Annual cycle of the west african
864 monsoon: regional circulations and associated water vapour transport. *Q. J. R. Meteorol. Soc.*,
865 **137**, <https://doi.org/DOI:10.1002/qj.728>.
- 866 Wainwright, C., L. C. Hiron, N. P. Klingaman, R. P. Allan, E. Black, and A. G. Turner, 2019:
867 The impact of air-sea coupling and ocean biases on the seasonal cycle of southern west african
868 precipitation. *Climate Dynamics*, **53**.
- 869 Wallace, J., 1975: Diurnal variations in precipitation and thunderstorm frequency over the conter-
870 minous united states. *Mon. Wea. Rev.*
- 871 Wallace, J., T. P. Mitchell, and C. Deser, 1989: The influence of sea-surface temperature on
872 surface wind in the eastern equatorial pacific: Seasonal and interannual variability. *J. Climat*,
873 [https://doi.org/https://doi.org/10.1175/1520-0442\(1989\)002<1492:TIOSST>2.0.CO;2](https://doi.org/https://doi.org/10.1175/1520-0442(1989)002<1492:TIOSST>2.0.CO;2).
- 874 Wang, G., and E. Eltahir, 2000: Role of vegetation dynamics in enhancing the low-frequency
875 variability of the sahel rainfall. *Water Resources Research*, **36(4)**, [https://doi.org/doi:10.1029/](https://doi.org/doi:10.1029/1999wr900361)
876 [1999wr900361](https://doi.org/doi:10.1029/1999wr900361)ˆ.
- 877 Weller, E., K. Shelton, M. Reeder, and C. Jakob, 2017: precipitation associated with convergence
878 lines. *J. Climate*.
- 879 Worou, K., H. Goosse, T. Fichefet, F. Guichard, and M. Diakhate, 2020: Interannual variability of
880 rainfall in the guinean coast region and its links with sea surface temperature changes over the
881 twentieth century for the different seasons. *Climate Dynamics*, [https://doi.org/https://doi.org/10.](https://doi.org/https://doi.org/10.1007/s00382-020-05276-5)
882 [1007/s00382-020-05276-5](https://doi.org/https://doi.org/10.1007/s00382-020-05276-5).
- 883 Yang, G., and J. Slingo, 2001: The diurnal cycle in the tropics. *Mon. Wea. Rev.*, [https://doi.org/](https://doi.org/https://doi.org/10.1175/1520-0493(2001)129<0784:TDCITT>2.0.CO;2)
884 [https://doi.org/10.1175/1520-0493\(2001\)129<0784:TDCITT>2.0.CO;2](https://doi.org/https://doi.org/10.1175/1520-0493(2001)129<0784:TDCITT>2.0.CO;2).
- 885 Zhang, G., and K. Cook, 2014: West african monsoon demise: Climatology, interannual variations,
886 and relationship to seasonal rainfall. *J. Geophys. Res. Atmos.*, **119,10**, [https://doi.org/doi:10.](https://doi.org/doi:10.1002/2014JD022043)
887 [1002/2014JD022043](https://doi.org/doi:10.1002/2014JD022043).
- 888 Zheng, X., E. Eltahir, and K. Emanuel, 1999: A mechanism relating tropical atlantic spring sea
889 surface temperature and west african rainfall. *QJRM*S, **125**.

Additional figures



892 FIG. A1. 2008-2015 climatology in May (left), June (middle) and July (right) of surface wind speed (black
 893 arrows, magnitude in shading, m/s) and SKT (black contours, intervals of 1°C) in ERA5 (top row) or observations
 894 (wind ASCAT and SST Reynolds, middle row), and their difference (bottom row).

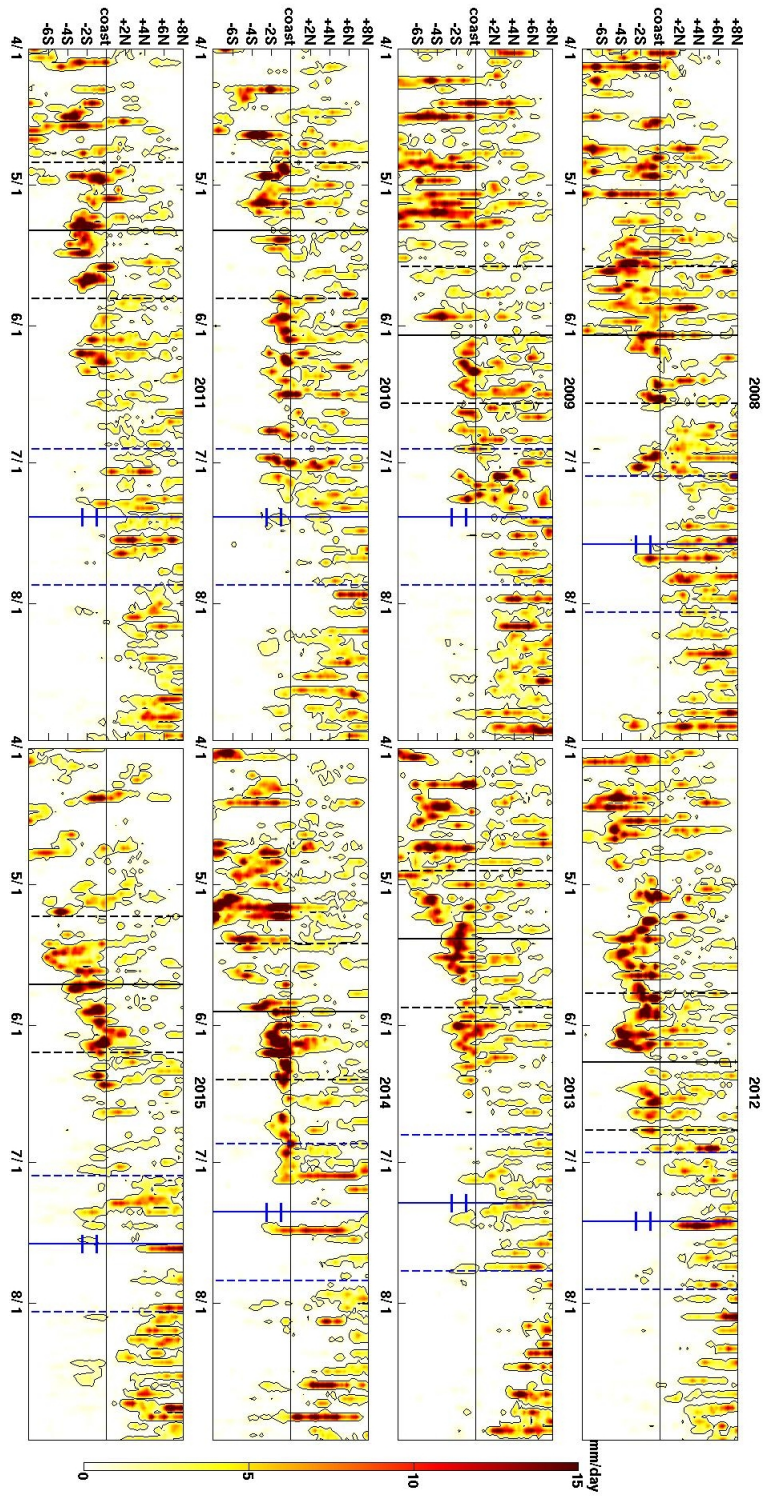
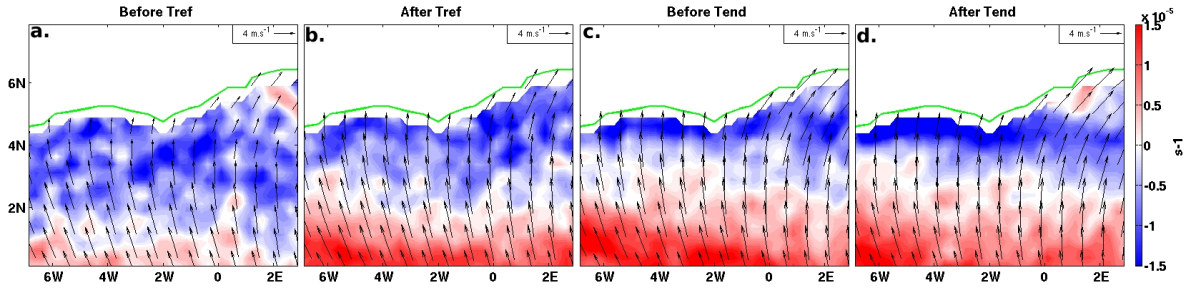


FIG. A2. Precipitation 1W-1E for all specific years between 2008 and 2015.



895 FIG. A3. Same as in Figure 3a and 3b, but for ASCAT surface wind and divergence, and before (c) / after (d)
 896 T_{end} as well as before (a) / after (b) T_{ref} .

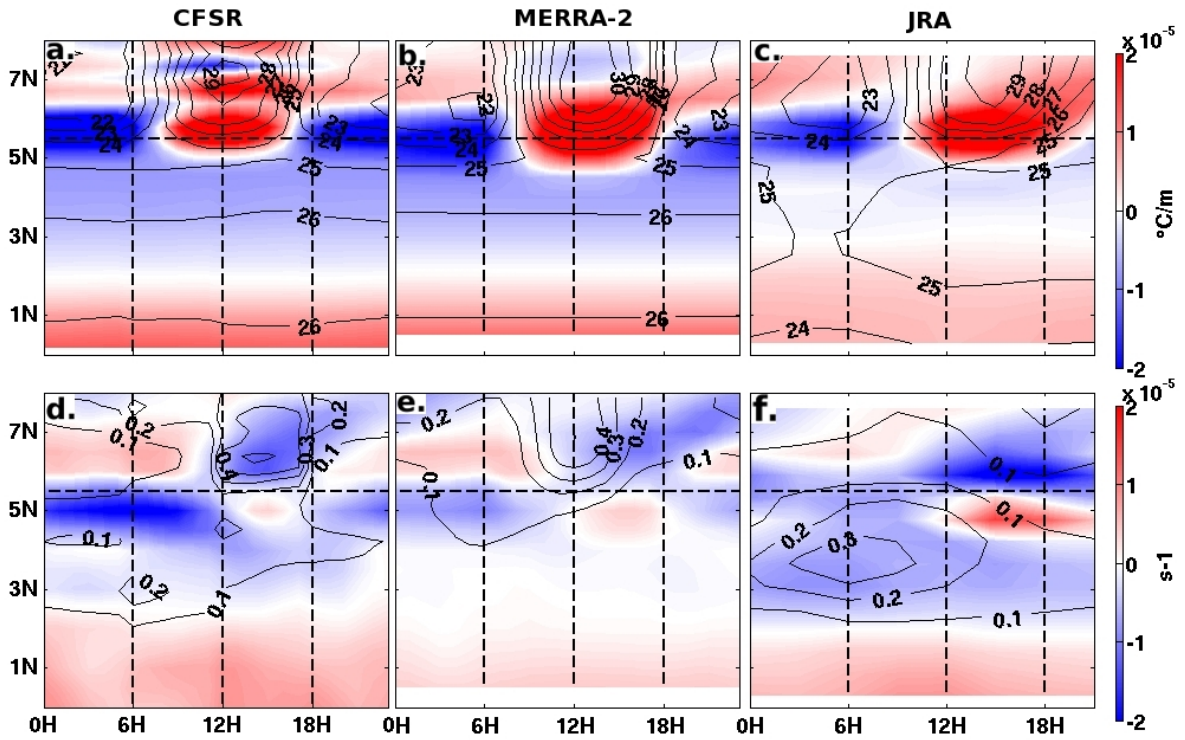


FIG. A4. Same as in Figure 8, but after Tend.